

The semi-explicit nonsmooth Newmark time integrator for robust unilateral contact in dynamic fragmentation simulations

Thibault Ghesquière-Diérickx¹, Guillaume Anciaux*¹, Vincent Acary², and Jean-François Molinari¹

¹Institute of Civil Engineering, Institute of Materials Science and Engineering, École Polytechnique Fédérale de Lausanne (EPFL), Lausanne, Switzerland

²INRIA, Université Grenoble Alpes, Grenoble, France

Abstract

Numerical simulations of solids undergoing dynamic fragmentation, a problem characterized by dynamic fracture and dense contacts, require accurately capturing the transition from a solid continuum to a collection of interacting fragments. We use the finite-element method with the extrinsic cohesive zone model for fracture. For contact, conventional penalty-based methods often exhibit numerical instabilities in dynamic collision-rich settings. To address this, we adapt and validate a novel semi-explicit time-integration scheme: the Nonsmooth Newmark (NSN) method for unilateral contact. Based on the Nonsmooth Contact Dynamics (NSCD) method, this formulation strongly enforces contact constraints at the velocity level. Within this scheme, the bulk dynamics are non-impulsive and integrated explicitly with second-order accuracy, and the fracture model allows displacement discontinuities and integrates the cohesive softening explicitly. Contact, treated rigorously as nonsmooth, is integrated implicitly with first-order accuracy. Benchmark tests demonstrate that the NSN scheme achieves accuracy comparable to established nonsmooth methods, such as the semi-explicit CD-Lagrange and implicit Moreau-Jean schemes. Moreover, it outperforms penalty-based approaches by orders of magnitude. Although the NSN method incurs a higher per-step computational cost, its enhanced stability allows for significantly larger time steps. Consequently, for 1D benchmarks, overall computational efficiency is comparable to or better than that of purely explicit approaches. We applied this framework to 1D fragmentation under free and confined expansion. Results reveal that confinement shifts the fracture energy budget from local fragment kinetic energy to larger-scale global system kinetic energy. Additionally, we found, counterintuitively, that, compared to fully elastic contact, adding contact dissipation reduces fracture energy yet increases the final fragment count. It occurs because such dissipation reduces the vibration within damaged fragments, allowing cleaner stress-wave propagation and better damage localization, driving cracks to full separation rather than distributing damage. These results establish the NSN scheme as a robust tool for generating high-fidelity fragmentation statistics.

Keywords: cohesive zone model; semi-explicit time integration; nonsmooth contact dynamics; dynamic fragmentation; penalty methods; contact mechanics; finite element method; nonsmooth newmark

1 Introduction

Systems characterized by dense, simultaneous contacts and impacts are omnipresent in both nature and engineering, spanning applications from granular flows and geophysical hazards such as rock avalanches to hypervelocity impacts, fragmentation, and mechanical assemblies. Among these, dynamic fracture is especially demanding: the contact interfaces emerge dynamically as surfaces are created, when the solid continuum undergoes rapid topological evolution, shattering into numerous discrete fragments. This process couples stress-wave-driven crack nucleation, growth, branching, and coalescence [1–4] with frequent, often simultaneous impacts between crack faces and fragments. This process of dynamic fragmentation occurs across vastly different scales—from the astronomical fragmentation of supernovae and planetary bodies [5], to fragmentation of spacecraft in orbit [6–9], and molecular DNA fragmentation under ion irradiation [10]. Such problems demand formulations capable of capturing both microsecond-scale fracture mechanics and long-term fragment dispersal. From a numerical perspective, accurately resolving this dual-timescale constraint requires millions of tiny integration steps, making numerical robustness a primary concern. Without a rigorous treatment of the nonsmooth mechanics associated with unilateral constraints and frictional laws that induce sharp discontinuities in velocity and forces, numerical artifacts can easily mask the underlying physics. The fidelity of the prediction of fragment kinematics depends, therefore, fundamentally on how the solid deformation, the fracture process, and contact interaction are discretized both in space and in time.

*Corresponding author: guillaume.anciaux@epfl.ch

Within the Finite Element Method (FEM) framework, fracture models are commonly grouped into diffuse and sharp-interface approaches. Diffuse models such as phase-field or lip-field [11–13], and related gradient-damage formulations represent cracks by a continuous damage field and are very robust for complex crack paths, but do not provide a geometrically sharp interface for contact and fragment tracking. Sharp methods, including the eXtended Finite Element Method (XFEM) [14], the cohesive zone model (CZM) [15–17], and discontinuous Galerkin (DG) methods combined with cohesive interfaces [18, 19], introduce displacement discontinuities along well-defined surfaces. We utilize the CZM because this sharp-crack topology is critical for tracking fragment kinematics and resolving post-fracture collisions. This method enables the spontaneous initiation and propagation of multiple cracks within the solid by inserting zero-thickness interface elements, called cohesive elements, along the boundaries of continuum elements [17]. We employ extrinsic CZMs [20], characterized by the absence of an initial cohesive stiffness: elements are inserted dynamically only when a fracture criterion is met. This approach contrasts with intrinsic models, in which predefined cohesive zones require a high dummy stiffness ($k \rightarrow \infty$) to enforce continuity before failure, thereby introducing artificial compliance that alters wave speeds [21]. By avoiding this initial stiffness entirely, the extrinsic approach maintains the exact elastic response of the bulk material until rupture. The robustness and scalability of explicit CZM have been successfully demonstrated in large-scale 3D fragmentation problems [20, 22–25]. In this work, we use the open-source and parallel *Akantu* FEM library [26] that incorporates extrinsic cohesive elements.

Accurately capturing contact and impact among crack faces and fragments is equally critical. Although contact mechanics are inherently nonsmooth, the contact constraints are typically regularized. Penalty-based methods approximate contact via artificial springs, preventing interpenetration between contacting bodies. These methods do not add additional degree-of-freedom (DOF) and naturally fit within explicit time-integration schemes, e.g., the Newmark scheme ($\beta = 0, \gamma = \frac{1}{2}$), that are required to accurately capture the wave-driven fracture process in dynamic fragmentation. However, such contact methods have a fundamental limitation. While low contact stiffness values allow unphysical interpenetration, high contact stiffness values severely restrict the stable time-step size of the explicit scheme, thereby prohibiting the efficient simulation of large systems [27, 28]. In addition, while the standard explicit Newmark scheme is symplectic and energy-conserving for smooth systems [29], the interaction between fracture and regularized contact introduces severe nonsmoothness in the loading paths. It leads to a persistent numerical energy drift that can compromise the simulation’s global stability. Our previous work [30] identified two potential mechanisms for this energy drift. As damage tends to zero, (i) the cohesive stiffness in tension diverges, and (ii) the sudden switch from tension (cohesion) to compression (contact) creates a discontinuous stiffness jump. The latter was identified as the main driver of global numerical instabilities. Previous efforts to mitigate these penalty-induced instabilities include bi-penalty formulations [31–33], mass redistribution schemes [34], and singular-mass adjustments [35]. These techniques remain partial fixes rather than fundamental resolutions of the underlying nonsmooth physics.

To overcome the instabilities of penalty-based methods, we build upon the Nonsmooth Contact Dynamics (NSCD) framework [36–39]. This approach strongly enforces the Signorini gap constraints at the velocity level and allows instantaneous velocity jumps upon impact. Standard “event-driven” nonsmooth solvers—which precisely locate every collision time by adapting the time step—are unsuitable for dynamic fragmentation due to the high density of impacts. Instead, a robust “time-stepping” approach is required [40]. Unlike regularized approaches that rely on single-valued force laws, the model employs set-valued force laws (solved as a mixed linear complementarity problem (MLCP) at each step) to determine contact impulses and post-impact velocities, thereby eliminating artificial compliance and associated energy drifts. Applying this logic to dynamic fragmentation requires a careful consideration of computational cost. While recent advancements have proposed a fully monolithic, purely implicit nonsmooth framework for CZM [41, 42], such an approach becomes computationally prohibitive for large-scale simulations. It is primarily due to the significant expansion of the system’s dimensionality through the introduction of Lagrange multipliers, as well as the challenges in parallelizing the solvers required to resolve the globally coupled systems.

After identifying contact as the primary driver of instability in regularized approaches, we aim to apply the implicit, nonsmooth treatment exclusively to contact surfaces, while retaining explicit integration for the bulk material and the fracture process. To that end, we adopt the nonsmooth Newmark (NSN) approach [43] and adapt it to such an explicit-implicit scheme. This targeted approach aims to contain computational cost: NSN solves only contact constraints, with cost scaling with the active contact set rather than the total system size. Crucially, the resulting linear complementarity problem (LCP) admits a convex quadratic programming (QP) formulation, enabling efficient, parallelizable implementations of the contact solver.

Beyond validating the new scheme against existing nonsmooth and penalty-based approaches, we present a dynamic fragmentation case study that targets a particularly challenging regime of dynamic fragmentation: post-fracture collisions between fragments in a confined environment. The standard 1D benchmark of dynamic fragmentation—the free expansion of a bar or Mott expanding ring—recovers classical trends in fragment size statistics and energy dissipation, validating the fracture model and its coupling with the NSN scheme. In contrast, enclosing fragments within rigid boundaries reveals how elastic fragment-wall and fragment-fragment collisions redistribute energy at the system scale, shifting the fracture

energy budget from the local, fragment-scale kinetic energy [44], to the global one. We further test the model by adding contact dissipation, i.e., inelastic collisions, and investigate how much energy is dissipated through fracture or through contact. These confined 1D tests stress-test the NSN contact formulation with dense, simultaneous contact events. The observed stability and energy control, achieved without the prohibitive cost of global implicit solves, demonstrate that the method can preserve physical fidelity in dense-contact scenarios, a key requirement for extension to orbital-debris-like scenarios, where frequent fragment–fragment interactions drive secondary fragmentation.

The remainder of this paper is organized as follows. Section 2 details the theoretical formulation of the semi-explicit NSN scheme and its algorithmic implementation as a quadratic programming (QP) problem. It also introduces a modified cohesive traction-separation law (TSL) that prevents prohibitively large cohesive stiffness, allowing for larger stable time steps. Section 3 presents a numerical validation of the proposed framework in terms of stability and efficiency. We study three simple benchmarks: the bouncing ball problem, the impact of a bar on a rigid wall, and the impact of a damaged bar on a rigid wall. These scenarios compare the NSN scheme with existing nonsmooth approaches (the implicit Moreau-Jean (MJ) [39] and the semi-explicit CD-Lagrange (CDL) [45]) and with the penalty-based approach. Finally, Section 4 applies the framework to 1D dynamic fragmentation. By comparing free and confined expansion, we demonstrate the framework’s readiness to handle and dense contact scenerios involving interacting cohesive cracks and complex multi-body interactions. This benchmark serves as a critical step toward higher dimensions. Section 5 concludes the paper and outlines future research directions.

2 Theoretical and numerical framework

The following section details the theoretical formulation of the semi-explicit NSN scheme and its algorithmic implementation as a QP problem. This framework is designed to handle elasticity, cohesive fracture, and unilateral contact. To ensure numerical stability and computational efficiency, we also introduce a modified cohesive TSL that prevents prohibitively large cohesive stiffness.

2.1 Variational formulation

Geometry of the problem. We consider an elastic body, Figure 1, occupying a reference configuration $\Omega \subset \mathbb{R}^d$ ($d = 1, 2, 3$). The current position is $\mathbf{x} = \mathbf{X} + \mathbf{u}(\mathbf{X}, t)$, where $\mathbf{X} \in \Omega$ denotes the material point in the reference configuration and $\mathbf{u}(\mathbf{X}, t)$ the displacement field at time $t \in [0, T]$. The boundary $\partial\Omega$ is decomposed into two disjoint parts

$$\partial\Omega = \Gamma^{\mathcal{D}} \cup \Gamma^{\mathcal{N}}, \quad (1)$$

where Dirichlet and Neumann boundary conditions are prescribed on $\Gamma^{\mathcal{D}}$ and $\Gamma^{\mathcal{N}}$, respectively. To account for cohesive fracture, we introduce a set of internal interfaces $\Gamma^{\text{coh}} \subset \bar{\Omega}$, with $\bar{\Omega} = \Omega \cup \partial\Omega$ the closure of the domain, along which the material may separate. Once an interface is created, two material points initially coinciding at $\mathbf{X} \in \Gamma^{\text{coh}}$ split into two distinct current positions \mathbf{x}^{\pm} on the two faces Γ^{\pm} of the interface. The displacement field may then be discontinuous, and we define the displacement jump as

$$\boldsymbol{\delta} := \llbracket \mathbf{u} \rrbracket = \mathbf{u}^+ - \mathbf{u}^-. \quad (2)$$

Let \mathbf{n} denote the unit normal to the interface, oriented from the “–” side to the “+” side. We decompose the displacement jump as

$$\delta_n := \boldsymbol{\delta} \cdot \mathbf{n}, \quad \boldsymbol{\delta}_t := (\mathbf{I} - \mathbf{n} \otimes \mathbf{n})\boldsymbol{\delta}, \quad (3)$$

so that δ_n is a scalar normal opening and $\boldsymbol{\delta}_t$ is the tangential (sliding) vector.

In addition to cohesive fracture, the body may come into frictionless unilateral contact either (i) between the two faces of a cohesive interface Γ^{coh} or (ii) between the external boundary $\Gamma^{\text{con}} \subset \partial\Omega$ and a rigid obstacle or another body. The normal gap function $g(\mathbf{u})$ measures the signed distance between the current configuration of a point on the contact surface and the obstacle along the outward unit normal \mathbf{n} . On cohesive interfaces, we have $g(\mathbf{u}) = \delta_n$. The unilateral contact constraint requires

$$g(\mathbf{u}) \geq 0 \quad \text{on } \Gamma^{\text{con}} \cup \Gamma^{\text{coh}}, \quad (4)$$

which excludes penetration of the obstacle and of the cohesive faces.

Principle of virtual power with cohesion and contact. Let \mathbf{v} be an admissible virtual velocity field and $\dot{\boldsymbol{\epsilon}}(\mathbf{v})$ its associated virtual strain rate. On cohesive interfaces, the virtual jump rate is

$$\dot{\boldsymbol{\delta}}(\mathbf{v}) := \llbracket \mathbf{v} \rrbracket = \mathbf{v}^+ - \mathbf{v}^-. \quad (5)$$

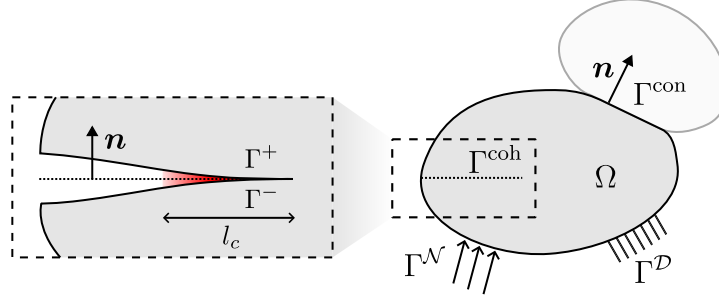


Figure 1: Geometry of the problem: Elastic body with Neumann boundary conditions on $\Gamma^{\mathcal{N}}$, Dirichlet boundary conditions on $\Gamma^{\mathcal{D}}$, cohesive interfaces on Γ^{coh} and unilateral contact on $\Gamma^{\text{con}} \cup \Gamma^{\text{coh}}$, both split into Γ^+ and Γ^-

The cohesive traction \mathbf{t}^{coh} is defined as the traction acting on the “+” face of the interface, exerted by the “-” face. The internal virtual power associated with bulk deformation and cohesive separation is

$$\mathcal{P}^{\text{int}}(\mathbf{v}) = - \int_{\Omega} \boldsymbol{\sigma} : \dot{\boldsymbol{\varepsilon}}(\mathbf{v}) dV + \int_{\Gamma^{\text{coh}}} \mathbf{t}^{\text{coh}} \cdot \boldsymbol{\delta}(\mathbf{v}) dS, \quad (6)$$

where $\boldsymbol{\sigma}$ is the Cauchy stress. Additional internal variables and their conjugate forces may be introduced. In the next section, we add damage through a thermodynamically consistent framework. The external and inertial virtual powers read

$$\mathcal{P}^{\text{ext}}(\mathbf{v}) = \int_{\Omega} \rho \mathbf{b} \cdot \mathbf{v} dV + \int_{\Gamma^{\mathcal{N}}} \mathbf{f}^{\text{ext}} \cdot \mathbf{v} dS, \quad \mathcal{P}^{\text{in}}(\mathbf{v}) = \int_{\Omega} \rho \ddot{\mathbf{u}} \cdot \mathbf{v} dV. \quad (7)$$

The *primal* statement of the principle of virtual power is:

$$\mathcal{P}^{\text{in}}(\mathbf{v}) = \mathcal{P}^{\text{ext}}(\mathbf{v}) + \mathcal{P}^{\text{int}}(\mathbf{v}) \quad \forall \mathbf{v} \in \mathcal{V}_0, \quad (8)$$

subject to the unilateral constraint $g(\mathbf{u}) \geq 0$. The space of admissible virtual velocities is

$$\mathcal{V}_0 = \{ \mathbf{v} \in H^1(\Omega \setminus \Gamma^{\text{coh}})^d \mid \mathbf{v} = \mathbf{0} \text{ on } \Gamma^{\mathcal{D}} \}. \quad (9)$$

To avoid handling the geometric constraint $g(\mathbf{u}) \geq 0$ directly in the primal space, we introduce a nonnegative Lagrange multiplier $\lambda \geq 0$ on $\Gamma^{\text{con}} \cup \Gamma^{\text{coh}}$, representing the normal contact pressure. The virtual power associated with the contact then reads

$$\mathcal{P}^{\text{con}}(\mathbf{v}; \lambda) = - \int_{\Gamma^{\text{con}} \cup \Gamma^{\text{coh}}} \lambda \dot{g}(\mathbf{v}) dS, \quad \dot{g}(\mathbf{v}) = (\mathbf{v}^+ - \mathbf{v}^-) \cdot \mathbf{n}. \quad (10)$$

The augmented virtual power balance is therefore

$$\mathcal{P}^{\text{in}}(\mathbf{v}) = \mathcal{P}^{\text{ext}}(\mathbf{v}) + \mathcal{P}^{\text{int}}(\mathbf{v}) + \mathcal{P}^{\text{con}}(\mathbf{v}; \lambda) \quad \forall \mathbf{v} \in \mathcal{V}_0. \quad (11)$$

Together with the kinematic constraint and dual admissibility, the primal-dual problem takes the form of the classical Signorini-Fichera complementarity conditions:

$$g(\mathbf{u}) \geq 0, \quad \lambda \geq 0, \quad \lambda g(\mathbf{u}) = 0 \quad \text{on } \Gamma^{\text{con}} \cup \Gamma^{\text{coh}}, \quad (12)$$

compactly written as $0 \leq g(\mathbf{u}) \perp \lambda \geq 0$ (where the symbol \perp indicates orthogonality/complementarity, i.e., the product $g\lambda = 0$) on $\Gamma^{\text{con}} \cup \Gamma^{\text{coh}}$. Using integration by parts in the bulk and along cohesive and contact surfaces, and assuming sufficient smoothness of the displacement and stress fields (e.g., $\mathbf{u} \in C^2(\Omega \setminus \Gamma^{\text{coh}})$ and $\boldsymbol{\sigma} \in C^1(\Omega \setminus \Gamma^{\text{coh}})$), as well as Lipschitz continuity of the boundaries, the primal-dual virtual power statement yields the following strong form

$$\begin{cases} \nabla \cdot \boldsymbol{\sigma} + \rho \mathbf{b} = \rho \ddot{\mathbf{u}} & \text{in } \Omega \setminus \Gamma^{\text{coh}}, \\ \mathbf{u} = \bar{\mathbf{u}} & \text{on } \Gamma^{\mathcal{D}}, \\ \boldsymbol{\sigma} \mathbf{n} = \mathbf{f}^{\text{ext}} & \text{on } \Gamma^{\mathcal{N}}, \\ \boldsymbol{\sigma} \mathbf{n} = -\lambda \mathbf{n} & \text{on } \Gamma^{\text{con}}, \\ \boldsymbol{\sigma}^{\pm} \mathbf{n} = \mathbf{t}^{\text{coh}} - \lambda \mathbf{n}, & \text{on } \Gamma^{\text{coh}}, \\ 0 \leq g(\mathbf{u}) \perp \lambda \geq 0 & \text{on } \Gamma^{\text{con}} \cup \Gamma^{\text{coh}}. \end{cases} \quad (13)$$

The constitutive structure of $(\boldsymbol{\sigma}, \mathbf{t}^{\text{coh}})$ will be specified in the next section through free energies, reversible state laws, and irreversible evolution equations, including a Camacho–Ortiz-type cohesive model with damage.

Free energy and reversible state laws. We consider the small-strain tensor $\boldsymbol{\varepsilon}$ in the bulk and the displacement jump $\boldsymbol{\delta}$ across cohesive interfaces as reversible state variables. To account for irreversible separation, a scalar internal damage variable $d \in (0, 1]$ is introduced on Γ^{coh} . The total free energy of the system reads

$$\Psi(\boldsymbol{\varepsilon}, \boldsymbol{\delta}, d) = \int_{\Omega} \Psi^e(\boldsymbol{\varepsilon}) dV + \int_{\Gamma^{\text{coh}}} \Psi^{\text{coh}}(\boldsymbol{\delta}, d) dS, \quad (14)$$

with Ψ^e the bulk elastic energy density and Ψ^{coh} the cohesive free energy density. Assuming linear elasticity of the bulk, the elastic energy density is given by

$$\Psi^e(\boldsymbol{\varepsilon}) = \frac{1}{2} \boldsymbol{\varepsilon} : \mathbf{C} : \boldsymbol{\varepsilon}, \quad (15)$$

with \mathbf{C} the fourth-order elasticity tensor. The reversible stress follows from the energy derivative:

$$\boldsymbol{\sigma} = \partial_{\boldsymbol{\varepsilon}} \Psi^e(\boldsymbol{\varepsilon}) = \mathbf{C} : \boldsymbol{\varepsilon}. \quad (16)$$

For the cohesive interfaces, we adopt a potential-based cohesive zone model (CZM). The mixed-mode effective measure characterizes the opening

$$\delta = \sqrt{\delta_n^2 + \beta^2 \|\boldsymbol{\delta}_t\|^2}, \quad (17)$$

where the dimensionless parameter β weighs the normal and tangential contributions. To reproduce the linear irreversible traction-separation law (TSL) of Camacho and Ortiz [20] within a thermodynamically consistent framework, we use the damage variable d and define the cohesive free energy density as

$$\Psi^{\text{coh}}(\boldsymbol{\delta}, d) = \frac{1}{2} \frac{1-d}{d} \frac{\sigma_c}{\delta_c} \delta^2, \quad (18)$$

where σ_c is the local cohesive strength and δ_c is the critical opening beyond which complete decohesion occurs. For a fixed d , this free energy generates a linear traction-separation response with secant stiffness

$$k(d) = \frac{1-d}{d} \frac{\sigma_c}{\delta_c}, \quad (19)$$

which coincides with the Camacho–Ortiz unloading/reloading stiffness. The associated cohesive traction follows from the chain rule:

$$\mathbf{t}^{\text{coh}} = \partial_{\boldsymbol{\delta}} \Psi^{\text{coh}}(\boldsymbol{\delta}, d) = \frac{1-d}{d} \frac{\sigma_c}{\delta_c} \frac{1}{\delta} (\delta_n \mathbf{n} + \beta^2 \boldsymbol{\delta}_t). \quad (20)$$

Dissipation and irreversible processes. We consider an isothermal setting in which the material response is decomposed into reversible and irreversible processes. The reversible response is fully characterized by the free energy Ψ introduced above. The bulk is assumed to be purely elastic, such that the mechanical dissipation vanishes in Ω :

$$\mathcal{D}^{\text{bulk}} = \boldsymbol{\sigma} : \dot{\boldsymbol{\varepsilon}} - \dot{\Psi}^e = 0. \quad (21)$$

Consequently, all dissipation is localized on the cohesive interfaces. On Γ^{coh} , the irreversible process is governed by the scalar internal variable d , which quantifies the loss of cohesive stiffness (damage). Although the physical fracture process involves the creation of new surfaces—a state of stored potential energy—the mechanical mechanism of decohesion is fundamentally irreversible ($\dot{d} \geq 0$). Because the energy required to break atomic bonds cannot be recovered as elastic potential, this structural change is treated as mechanical dissipation within the continuum framework, governed by the local Clausius-Duhem inequality:

$$\mathcal{D}^{\text{coh}} = \mathbf{t}^{\text{coh}} \cdot \dot{\boldsymbol{\delta}} - \dot{\Psi}^{\text{coh}}(\boldsymbol{\delta}, d) \geq 0. \quad (22)$$

Using the state law $\mathbf{t}^{\text{coh}} = \partial_{\boldsymbol{\delta}} \Psi^{\text{coh}}$ and applying the chain rule to the free energy Ψ^{coh} , the dissipation reduces to a concise form:

$$\mathcal{D}^{\text{coh}} = -\partial_d \Psi^{\text{coh}}(\boldsymbol{\delta}, d) \dot{d} = G \dot{d} \geq 0. \quad (23)$$

The irreversible damage process is therefore driven by the thermodynamic force G conjugate to damage d , which is identified as the cohesive energy release rate:

$$G = -\partial_d \Psi^{\text{coh}}(\boldsymbol{\delta}, d) = \frac{1}{2} \frac{\sigma_c}{\delta_c} \frac{\delta^2}{d^2} \geq 0. \quad (24)$$

At complete decohesion ($d = 1, \delta = \delta_c$), this energy release rate reaches its critical fracture toughness value $G_c = \sigma_c \delta_c / 2$. To ensure $\mathcal{D}^{\text{coh}} \geq 0$, the damage evolution must satisfy $\dot{d} \geq 0$. This irreversibility condition is typically enforced through a rate-independent evolution law based on a loading function

$$f(\boldsymbol{\delta}, d) := \frac{\delta}{\delta_c} - d \leq 0 \quad \Leftrightarrow \quad \frac{\delta}{\delta_c} \leq d. \quad (25)$$

From the Kuhn–Tucker conditions associated with this constraint, we have

$$\dot{d} \geq 0, \quad f(\delta, d) \leq 0, \quad \dot{d} f(\delta, d) = 0, \quad (26)$$

which ensures that damage grows only when the loading function reaches zero, i.e., when $\delta = d \delta_c$. These conditions are equivalent to the classical Camacho–Ortiz decohesion criterion that introduces the history-dependent evolution law

$$\delta_{\max}(t) := \max_{0 \leq \tau \leq t} \delta(\tau), \quad d(t) := \frac{\delta_{\max}(t)}{\delta_c}, \quad (27)$$

ensuring that damage increases only when the current opening δ attains a new maximum.

2.2 Space and time discretization

Space discretization. The spatial discretization is carried out using standard finite elements. The displacement field is approximated as $\mathbf{u}(\mathbf{x}, t) \approx \sum_{i=1}^n \mathbf{N}_i(\mathbf{x}) \mathbf{u}_i(t)$, where $\mathbf{N}_i(\mathbf{x})$ are the shape functions and $\mathbf{u}_i(t)$ are the nodal displacements, with duplicate nodes along Γ^{coh} to capture displacement jumps. The contact pressure is discretized by piecewise constant Lagrange multipliers defined at the contact nodes on $\Gamma^{\text{con}} \cup \Gamma^{\text{coh}}$. Inserting these approximations into the virtual power principle, choosing nodal basis functions as test functions, and assembling over all elements and interface elements, we obtain the semi-discrete equation of motion

$$\mathbf{M} \dot{\mathbf{v}}(t) + \mathbf{K}(\mathbf{d}) \mathbf{u}(t) = \mathbf{f}^{\text{ext}}(t) + \mathbf{H}^\top \boldsymbol{\lambda}(t), \quad \mathbf{v}(t) = \dot{\mathbf{u}}(t). \quad (28)$$

In this system, $\mathbf{M} \in \mathbb{R}^{n \times n}$ is the mass matrix. The matrix $\mathbf{K} \in \mathbb{R}^{n \times n}$ is the stiffness matrix that collects the bulk and cohesive contributions. It is explicitly state-dependent, as indicated by \mathbf{d} , which represents the history of cohesive damage variables. These variables are updated locally at the interface integration points to satisfy the irreversibility condition ($\dot{d} \geq 0$) of the damage process before the global matrix is assembled. The vector $\mathbf{f}^{\text{ext}}(t) \in \mathbb{R}^n$ collects the external forces. The terms related to contact involve the matrix $\mathbf{H} \in \mathbb{R}^{m \times n}$ and the vector of nonnegative contact pressures $\boldsymbol{\lambda}(t) \in \mathbb{R}^m$, where m is the number of contact nodes. The matrix \mathbf{H} maps nodal displacements to normal gaps $\mathbf{g}(t) \in \mathbb{R}^m$ via

$$\mathbf{g}(t) = \mathbf{H} \mathbf{u}(t). \quad (29)$$

The physical requirement of non-penetration is then enforced through the discrete complementarity conditions:

$$0 \leq \mathbf{g}(t) \perp \boldsymbol{\lambda}(t) \geq 0. \quad (30)$$

Time discretization Unilateral contact can induce discontinuities in the velocities of finite-dimensional dynamical systems. At such impact events, a contact force $\boldsymbol{\lambda}(t) \in L^1$ cannot produce an instantaneous change in velocity. To account for this impulsive behavior, the time discretization must be carefully designed [39], and the reaction forces must be treated as vector-valued measures. The equations of motion (28) are rewritten in distributional form, an equality of measures, as

$$\mathbf{M} d\mathbf{v}(t) + \mathbf{K} \mathbf{u}(t) dt = \mathbf{f}^{\text{ext}}(t) dt + \mathbf{H}^\top d\mathbf{i}(t). \quad (31)$$

Because impacts cause velocity jumps, the velocity \mathbf{v} is a function of bounded variation; its distributional derivative $d\mathbf{v}$ therefore comprises an absolutely continuous term and an atomic term supported on the countable set of collision times $\{t_c\}$. The contact impulse measure $d\mathbf{i}$ has the same structure.

Equating the terms that are absolutely continuous with respect to the Lebesgue measure dt yields the standard smooth equations of motion. The corresponding densities are the acceleration $\dot{\mathbf{v}}(t)$ for $d\mathbf{v}$ and the contact force $\boldsymbol{\lambda}(t)$ for $d\mathbf{i}$, giving

$$\mathbf{M} \dot{\mathbf{v}}(t) + \mathbf{K} \mathbf{u}(t) = \mathbf{f}^{\text{ext}}(t) + \mathbf{H}^\top \boldsymbol{\lambda}(t), \quad (32)$$

valid almost everywhere. Equivalently, equating the atomic terms concentrated on $\{t_c\}$ gives the momentum balance at impact. Their densities are defined with respect to the sum of Dirac measures $\sum_c \delta_{t_c}$, where δ_{t_c} is the Dirac measure centered at t_c . For $d\mathbf{v}$, this density is the velocity jump $\llbracket \mathbf{v} \rrbracket(t_c) = \mathbf{v}(t_c^+) - \mathbf{v}(t_c^-)$, and for $d\mathbf{i}$, it is the contact impulse $\mathbf{j}(t_c) \geq 0$. This yields the momentum balance at impact:

$$\mathbf{M} \llbracket \mathbf{v} \rrbracket(t_c) = \mathbf{H}^\top \mathbf{j}(t_c). \quad (33)$$

In this finite-dimensional setting, this impact equation is underdetermined (n equations, $n + m$ unknowns, i.e., the post-impact velocities and the contact impulses). To close the system, we use Newton’s impact law to relate the pre- and post-impact velocities. At t_c , the gap closes $\mathbf{H} \mathbf{u}(t_c) = 0$ with negative relative velocity $\mathbf{H} \mathbf{v}(t_c^-) < 0$, the impact law reads

$$0 \leq \mathbf{j}(t_c) \perp \mathbf{H} \mathbf{v}(t_c^+) + e \mathbf{H} \mathbf{v}(t_c^-) \geq 0, \quad (34)$$

with $e \in [0, 1]$ the coefficient of restitution. It phenomenologically captures the energy dissipation inherent in the collision, aggregating effects such as material plasticity, microcracking, acoustic emission, and heat generation into a constitutive relation.

We can employ several time-stepping strategies to integrate the nonsmooth equations of motion. A widely used approach is the *Moreau-Jean scheme* [36–39], which consists of integrating the distributional form of the momentum balance over each time interval $[t_n, t_{n+1}]$. This integration yields a first-order-accurate method for the velocities, while the displacements are updated using the θ -method. In contrast, the technique adopted here follows the *nonsmooth Newmark scheme* introduced by Chen et al. [43]. The key idea is an algorithmic split of the dynamics into two parts: a contribution $\tilde{\square}$ associated with bulk deformation, external loading, and cohesive fracture, and a contribution $\hat{\square}$ that gathers the entire contact reaction. By an abuse of terminology, we shall refer to the former as the “smooth” part and to the latter as the “nonsmooth” part.

Following Chen et al. [43], the velocity measure is split so that the smooth part $\dot{\tilde{\mathbf{v}}} dt$ contains only the free-flight inertial and internal terms, while the nonsmooth remainder $d\hat{\mathbf{v}}$ carries all contact-induced velocity changes. Thus the full contact measure $d\mathbf{i}$ —comprising both the absolutely continuous contact forces (density $\boldsymbol{\lambda}(t)$) and the atomic impulses at impact times—is gathered in the nonsmooth side. This assignment differs from the Lebesgue decomposition introduced earlier, and yields the split dynamics

$$\begin{cases} \mathbf{M}\dot{\tilde{\mathbf{v}}} dt + \mathbf{K}\mathbf{u}(t) dt = \mathbf{f}^{\text{ext}}(t) dt & \text{(Smooth dynamics)} \\ \mathbf{M}d\hat{\mathbf{v}} = \mathbf{H}^\top d\mathbf{i}(t) & \text{(Nonsmooth dynamics)} \end{cases} \quad (35)$$

The smooth part is discretized using a second-order explicit Newmark- β scheme (with $\beta = 0$ and $\gamma = 1/2$), while the nonsmooth part employs a first-order implicit Euler scheme. The discrete smooth acceleration $\dot{\tilde{\mathbf{v}}}_{n+1}$ satisfies

$$\mathbf{M}\dot{\tilde{\mathbf{v}}}_{n+1} + \mathbf{K}\mathbf{u}_{n+1} = \mathbf{f}_{n+1}^{\text{ext}}. \quad (36)$$

The impulsive velocity increment $\hat{\mathbf{v}}_{n+1}$ is obtained by approximating the integral of the nonsmooth measure over the time step $[t_n, t_{n+1}]$:

$$\mathbf{M}\hat{\mathbf{v}}_{n+1} \approx \mathbf{H}^\top \mathbf{p}_{n+1}, \quad (37)$$

where \mathbf{p}_{n+1} is the total contact impulse accumulated during the time step, comprising both the integral of the contact forces and the sum of discrete impact impulses. To close the system, Newton’s impact law is enforced over the active constraint set $\mathcal{A} = \{i \in \{1, \dots, m\} : g_i \leq 0\}$, where \mathbf{g} is a gap prediction vector that identifies potential contact points. This prediction depends on the specific time-integration scheme and can be based on either the gap at the previous time step, t_n , or a predicted gap at t_{n+1} . We define $\mathbf{H}^{\mathcal{A}} \in \mathbb{R}^{|\mathcal{A}| \times n}$ as the submatrix of \mathbf{H} restricted to the rows corresponding to the indices in \mathcal{A} . Similarly, $\mathbf{p}_{n+1}^{\mathcal{A}} \in \mathbb{R}^{|\mathcal{A}|}$ is the reduced impulse vector for these active constraints. The discretized impact law is then expressed as:

$$\mathbf{0} \leq \mathbf{p}_{n+1}^{\mathcal{A}} \perp \mathbf{H}^{\mathcal{A}}\mathbf{v}_{n+1} + e(\mathbf{H}^{\mathcal{A}}\mathbf{v}_n) \geq \mathbf{0}. \quad (38)$$

By restricting the complementarity condition to \mathcal{A} , we ensure that impulses $p_{n+1,i}$ are identically zero for all inactive constraints $i \notin \mathcal{A}$. Following this discretization, the smooth displacements and velocities are updated using the acceleration variable $\mathbf{a} = \tilde{\mathbf{v}}$:

$$\begin{cases} \tilde{\mathbf{u}}_{n+1} = \mathbf{u}_n + \Delta t \mathbf{v}_n + \frac{\Delta t^2}{2} \mathbf{a}_n, \\ \tilde{\mathbf{v}}_{n+1} = \mathbf{v}_n + \frac{\Delta t}{2} (\mathbf{a}_n + \mathbf{a}_{n+1}). \end{cases} \quad (39)$$

This smooth state serves as the “free” configuration to predict the active contact set \mathcal{A} . Specifically, we define the predicted gap as $\mathbf{g} = \mathbf{H}\tilde{\mathbf{u}}_{n+1}$, and identify all indices i such that $g_i \leq 0$. To account for impulsive terms within $[t_n, t_{n+1}]$, the nonsmooth correction $\hat{\mathbf{v}}_{n+1}$ is added to the smooth predictions:

$$\begin{cases} \mathbf{u}_{n+1} = \tilde{\mathbf{u}}_{n+1} + \frac{\Delta t}{2} \hat{\mathbf{v}}_{n+1}, \\ \mathbf{v}_{n+1} = \tilde{\mathbf{v}}_{n+1} + \hat{\mathbf{v}}_{n+1}. \end{cases} \quad (40)$$

The resulting semi-explicit nonsmooth Newmark (NSN) time integration scheme for unilateral contact with impacts is summarized below.

$$\begin{cases} \mathbf{M}\mathbf{a}_{n+1} + \mathbf{K}\mathbf{u}_{n+1} = \mathbf{f}_{n+1}^{\text{ext}} & (41a) \\ \mathbf{M}\hat{\mathbf{v}}_{n+1} = (\mathbf{H}^{\mathcal{A}})^\top \mathbf{p}_{n+1}^{\mathcal{A}} & (41b) \\ \mathbf{0} \leq \mathbf{p}_{n+1}^{\mathcal{A}} \perp \mathbf{H}^{\mathcal{A}}\mathbf{v}_{n+1} + e\mathbf{H}^{\mathcal{A}}\mathbf{v}_n \geq \mathbf{0}, \quad \text{with } \mathcal{A} = \{i \mid g_i(\tilde{\mathbf{u}}_{n+1}) \leq 0\} & (41c) \\ \tilde{\mathbf{u}}_{n+1} = \mathbf{u}_n + \Delta t \mathbf{v}_n + \frac{\Delta t^2}{2} \mathbf{a}_n & (41d) \\ \tilde{\mathbf{v}}_{n+1} = \mathbf{v}_n + \frac{\Delta t}{2} (\mathbf{a}_n + \mathbf{a}_{n+1}) & (41e) \\ \mathbf{u}_{n+1} = \tilde{\mathbf{u}}_{n+1} + \frac{\Delta t}{2} \hat{\mathbf{v}}_{n+1} & (41f) \\ \mathbf{v}_{n+1} = \tilde{\mathbf{v}}_{n+1} + \hat{\mathbf{v}}_{n+1} & (41g) \end{cases}$$

2.3 Formulation as a constrained optimization problem

Solving the system (41a)–(41g) requires handling the coupling between the smooth and nonsmooth dynamics. To this end, we reformulate the problem as a linear complementarity problem (LCP) restricted to the active set \mathcal{A} . With unknowns \mathbf{a}_{n+1} and $\mathbf{p}_{n+1}^{\mathcal{A}}$, we rewrite the system to feed it to a dedicated solver.

From the nonsmooth relation (41b), we express the contact-induced velocity jump as

$$\widehat{\mathbf{v}}_{n+1} = \mathbf{M}^{-1} (\mathbf{H}^{\mathcal{A}})^{\top} \mathbf{p}_{n+1}^{\mathcal{A}}. \quad (42)$$

Substituting this expression into the kinematic updates (41f)–(41g) yields

$$\mathbf{u}_{n+1} = \widetilde{\mathbf{u}}_{n+1} + \frac{\Delta t}{2} \mathbf{M}^{-1} (\mathbf{H}^{\mathcal{A}})^{\top} \mathbf{p}_{n+1}^{\mathcal{A}}, \quad (43a)$$

$$\mathbf{v}_{n+1} = \mathbf{v}_n + \frac{\Delta t}{2} (\mathbf{a}_n + \mathbf{a}_{n+1}) + \mathbf{M}^{-1} (\mathbf{H}^{\mathcal{A}})^{\top} \mathbf{p}_{n+1}^{\mathcal{A}}. \quad (43b)$$

Inserting (43a)–(43b) into the equilibrium (41a) and the impact law (41c) results in a mixed linear complementarity problem in the unknown pair $(\mathbf{a}_{n+1}, \mathbf{p}_{n+1}^{\mathcal{A}})$:

$$\mathbf{M}\mathbf{a}_{n+1} + \frac{\Delta t}{2} \mathbf{K}\mathbf{M}^{-1} (\mathbf{H}^{\mathcal{A}})^{\top} \mathbf{p}_{n+1}^{\mathcal{A}} + \mathbf{K}\widetilde{\mathbf{u}}_{n+1} - \mathbf{f}_{n+1}^{\text{ext}} = \mathbf{0}, \quad (44a)$$

$$\mathbf{0} \leq \frac{\Delta t}{2} \mathbf{H}^{\mathcal{A}} \mathbf{a}_{n+1} + \mathbf{H}^{\mathcal{A}} \mathbf{M}^{-1} (\mathbf{H}^{\mathcal{A}})^{\top} \mathbf{p}_{n+1}^{\mathcal{A}} + \mathbf{H}^{\mathcal{A}} \left(\frac{\Delta t}{2} \mathbf{a}_n + (1+e) \mathbf{v}_n \right) \perp \mathbf{p}_{n+1}^{\mathcal{A}} \geq \mathbf{0}. \quad (44b)$$

Eliminating the acceleration \mathbf{a}_{n+1} from the equilibrium equation (44a) and substituting the result into the complementarity condition (44b) yields a standard linear complementarity problem (LCP) in the contact impulse alone:

$$\mathbf{0} \leq \mathbf{W}' \mathbf{p}_{n+1}^{\mathcal{A}} + \mathbf{b} \perp \mathbf{p}_{n+1}^{\mathcal{A}} \geq \mathbf{0}, \quad (45)$$

with the modified Delassus operator and the right-hand side given directly by

$$\mathbf{W}' := \mathbf{H}^{\mathcal{A}} \mathbf{M}^{-1} \left[\mathbf{I} - \frac{\Delta t^2}{4} \mathbf{K}\mathbf{M}^{-1} \right] (\mathbf{H}^{\mathcal{A}})^{\top}, \quad (46)$$

$$\mathbf{b} := \mathbf{H}^{\mathcal{A}} \left[(1+e) \mathbf{v}_n + \frac{\Delta t}{2} \mathbf{a}_n - \frac{\Delta t}{2} \mathbf{M}^{-1} (\mathbf{K}\widetilde{\mathbf{u}}_{n+1} - \mathbf{f}_{n+1}^{\text{ext}}) \right] \quad (47)$$

Defining the contact-free velocity predictor

$$\mathbf{v}_{n+1}^{\text{free}} := \mathbf{v}_n + \frac{\Delta t}{2} \mathbf{a}_n + \frac{\Delta t}{2} \mathbf{M}^{-1} (\mathbf{f}_{n+1}^{\text{ext}} - \mathbf{K}\widetilde{\mathbf{u}}_{n+1}), \quad (48)$$

the vector \mathbf{b} can be written compactly as $\mathbf{b} = \mathbf{H}^{\mathcal{A}} (\mathbf{v}_{n+1}^{\text{free}} + e\mathbf{v}_n)$. Whenever \mathbf{W}' is symmetric positive semidefinite (SPSD), this LCP is equivalent to the convex quadratic programming (QP) over the active set:

$$\min_{\mathbf{p}_{n+1}^{\mathcal{A}} \geq \mathbf{0}} \frac{1}{2} (\mathbf{p}_{n+1}^{\mathcal{A}})^{\top} \mathbf{W}' \mathbf{p}_{n+1}^{\mathcal{A}} + (\mathbf{p}_{n+1}^{\mathcal{A}})^{\top} \mathbf{b}. \quad (49)$$

As shown in Appendix A, a sufficient condition for \mathbf{W}' to be SPSPD is that the time step satisfies

$$\Delta t \leq \frac{2}{\omega_{\max}}, \quad (50)$$

where ω_{\max} denotes the largest natural frequency of the system that the contact subspace excites. The standard central-difference stability bound can be used as a safe choice. The predictor–corrector semi-explicit NSN scheme is summarized in Algorithm 1.

2.4 Modified traction-separation law (TSL)

Unlike the formulation in [41, 42], where the decohesion process is treated through a complementarity condition, similar to (26), our model integrates decohesion explicitly by introducing the history variable δ_{\max} (27). This choice is motivated by a key observation in [30]: the discontinuity in the cohesive traction at softening events, i.e., when $\dot{d} > 0$, does not introduce any instability, as the energy error due to this jump is exactly compensated by the energy dissipated through

Algorithm 1: Predictor–corrector explicit NSN with QP contact solve

Input: $\mathbf{u}_0, \mathbf{v}_0, \mathbf{a}_0, \Delta t, e, t_{\text{end}}, \mathbf{M}, \mathbf{K}, \mathbf{H}, \{\mathbf{f}_n^{\text{ext}}\}_{n \geq 0}$
Output: Trajectory $\{\mathbf{u}_n, \mathbf{v}_n, \mathbf{a}_n\}$
 $t \leftarrow 0, n \leftarrow 0$
while $t < t_{\text{end}}$ **do**
 $t \leftarrow t + \Delta t, \quad n \leftarrow n + 1$
 $\tilde{\mathbf{u}}_{n+1} \leftarrow \mathbf{u}_n + \Delta t \mathbf{v}_n + \frac{\Delta t^2}{2} \mathbf{a}_n \quad // (41d)$

 Update \mathbf{d} from $\tilde{\mathbf{u}}_{n+1}$ and assemble $\mathbf{K}(\mathbf{d})$

 Gap prediction $\mathbf{g}_{n+1} \leftarrow \mathbf{H}\tilde{\mathbf{u}}_{n+1} \quad // (29)$

 Active set $\mathcal{A} = \{i \mid g_i(\tilde{\mathbf{u}}_{n+1}) \leq 0\}$
if $\mathcal{A} = \emptyset$ **then**

 No contact case: smooth update with $\hat{\mathbf{v}}_{n+1} = \mathbf{0}$
 $\mathbf{u}_{n+1} \leftarrow \tilde{\mathbf{u}}_{n+1} \quad // (41f)$
 $\mathbf{a}_{n+1} \leftarrow \mathbf{M}^{-1}(\mathbf{f}_{n+1}^{\text{ext}} - \mathbf{K} \mathbf{u}_{n+1}) \quad // (41a)$
 $\mathbf{v}_{n+1} \leftarrow \mathbf{v}_n + \frac{\Delta t}{2}(\mathbf{a}_n + \mathbf{a}_{n+1}) \quad // (41e)$
else

Active contact case: solve QP for contact impulses

 Restrict \mathbf{H} to the active set $\mathbf{H}^{\mathcal{A}}$

 Assemble operators \mathbf{W}' and \mathbf{b} // (47)
 $\mathbf{W}' \leftarrow \mathbf{H}^{\mathcal{A}} \mathbf{M}^{-1} \left[\mathbf{I} - \frac{\Delta t^2}{4} \mathbf{K} \mathbf{M}^{-1} \right] (\mathbf{H}^{\mathcal{A}})^{\top}$
 $\mathbf{b} \leftarrow \mathbf{H}^{\mathcal{A}} \left[(1+e) \mathbf{v}_n + \frac{\Delta t}{2} \mathbf{a}_n - \frac{\Delta t}{2} \mathbf{M}^{-1} (\mathbf{K} \tilde{\mathbf{u}}_{n+1} - \mathbf{f}_{n+1}^{\text{ext}}) \right]$

 Solve the QP: $\mathbf{p}_{n+1}^{\mathcal{A}} \leftarrow \arg \min_{\mathbf{p} \geq 0} \frac{1}{2} \mathbf{p}^{\top} \mathbf{W}' \mathbf{p} + \mathbf{p}^{\top} \mathbf{b} \quad // (49)$

 Velocity correction: $\hat{\mathbf{v}}_{n+1} \leftarrow \mathbf{M}^{-1} (\mathbf{H}^{\mathcal{A}})^{\top} \mathbf{p}_{n+1}^{\mathcal{A}} \quad // (41b)$

Nonsmooth update

 $\mathbf{u}_{n+1} \leftarrow \tilde{\mathbf{u}}_{n+1} + \frac{\Delta t}{2} \hat{\mathbf{v}}_{n+1} \quad // (41f)$
 $\mathbf{v}_{n+1} \leftarrow \tilde{\mathbf{v}}_{n+1} + \hat{\mathbf{v}}_{n+1} \quad // (41g)$
 $\mathbf{a}_{n+1} \leftarrow \mathbf{M}^{-1} (\mathbf{f}_{n+1}^{\text{ext}} - \mathbf{K} \mathbf{u}_{n+1}) \quad // (41a)$

Advance

 $\mathbf{u}_n \leftarrow \mathbf{u}_{n+1}, \mathbf{v}_n \leftarrow \mathbf{v}_{n+1}, \mathbf{a}_n \leftarrow \mathbf{a}_{n+1}$

decohesion. It allows us to preserve the high performance and simplicity of the explicit framework. However, while extrinsic cohesive zone models typically assume a rigid pre-fracture state, their implementation in an explicit dynamic framework introduces a critical numerical challenge during the onset of softening. As damage d approaches zero, the secant stiffness $k(d)$ tends toward infinity (19). In explicit schemes, where the stable time step Δt is inversely proportional to the square root of the maximum system stiffness (50), this results in a vanishingly small Δt , rendering the simulation computationally infeasible. The contact implementation adopted here relies on the convexity of the underlying minimization problem (49). Because this convexity is lost when the stability condition is violated, and to avoid the need for impractically small time steps, we introduce a regularization of the traction-separation law by imposing a stiffness cap \tilde{k} . By setting the stiffness to zero (constant traction unloading) when $k > \tilde{k}$, we prevent the time step from dropping below a usable threshold, usually governed by the bulk material. Our capped law retains a secant unloading path whenever $k < \tilde{k}$.

To implement this regularized law, we link the globally defined stiffness threshold to a local damage threshold \tilde{d} with $\tilde{k} = T(\tilde{d})/(\tilde{d}\delta_c)$. With the traction scalar function $T(d)$ defined as

$$T(d) = \sigma_c(1 - d), \quad (51)$$

the damage threshold reads

$$\tilde{d} = \frac{\sigma_c}{\sigma_c + \tilde{k}\delta_c}. \quad (52)$$

Therefore, we split the law into two regimes and express the cohesive traction as

$$\mathbf{t}^{\text{coh}} = \begin{cases} \sigma_c(1 - d) \frac{(\delta_n \mathbf{n} + \beta^2 \delta_t)}{\|(\delta_n \mathbf{n} + \beta^2 \delta_t)\|}, & \text{if } d < \tilde{d}, \\ \frac{1-d}{d} \frac{\sigma_c}{\delta_c} \frac{1}{\delta} (\delta_n \mathbf{n} + \beta^2 \delta_t), & \text{if } d \geq \tilde{d}, \end{cases} \quad (53)$$

to which the irreversibility condition (27) still applies. This modified law is illustrated in Figure 2.

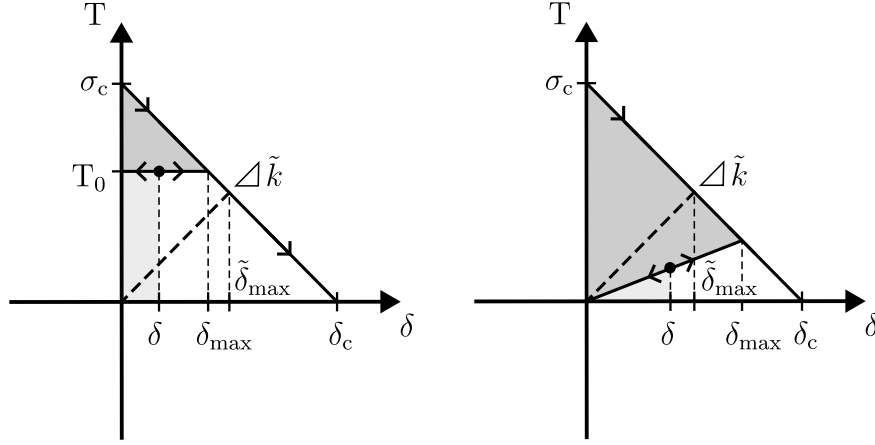


Figure 2: Modified traction-separation law with capped stiffness $\tilde{k} = k(\tilde{d})$.

The modified law affects the response of low-damage cohesive elements. The energy required to open at constant traction exceeds that required to open along a linear unloading/reloading path. We expect this effect to be negligible at high strain rates but potentially more significant at low strain rates. Indeed, a higher strain rate leads to greater initial damage in the cohesive elements, thereby causing overshooting of the regularized regime. The value of \tilde{k} should be chosen high enough to minimize this effect. We can choose this value based on a fraction of the characteristic stiffness of a bulk element: $\tilde{k} = \alpha \frac{E}{h_e}$ with h_e the characteristic size of a bulk element and α a user-defined parameter. For the simulations presented in this work using the nonsmooth contact implementation, we set $\alpha \in [1, 10]$ to minimize the effect of the modified law on the overall response while maintaining a practical time step.

3 Numerical validation

In this section, we validate the proposed semi-explicit NSN scheme using three benchmark problems: the bouncing ball, the impacting bar, and the impacting bar with internal damage. The classical bouncing ball—a single degree-of-freedom (SDOF) system with rigid impact—serves as a fundamental test of the algorithm’s accuracy in capturing impact and restitution phenomena. The second benchmark simulates the impact of a multi-degree-of-freedom bar against a rigid wall. For both benchmarks, the results are compared against the analytical solutions as well as two established nonsmooth contact dynamics schemes: the implicit Moreau-Jean (MJ) scheme (with $\theta = \frac{1}{2}$) [39] and the semi-explicit CD-Lagrange (CDL) scheme [45]. We further evaluate the NSN scheme against a traditional penalty-based contact formulation within the standard explicit Newmark- β scheme (with $\beta = 0$, $\gamma = \frac{1}{2}$). For this purpose, and to model a case characteristic of dynamic fragmentation, the impacting bar problem is modified by introducing internal damage within the bar to represent a fragment that drifts after fragmentation and strikes a rigid obstacle.

3.1 Bouncing ball

This problem focuses on the impact of a SDOF system (a ball) on a rigid surface under the influence of gravity. The ball is modeled as a point mass m with an initial height u_0 and zero initial velocity $v_0 = 0$. When the ball impacts the rigid surface at $u = 0$, it undergoes an instantaneous change in velocity governed by the coefficient of restitution e , which defines the ratio of the post-impact relative velocity to the pre-impact relative velocity. The analytical solution for the ball’s motion consists of a series of parabolic trajectories between impacts, where the time of each bounce and the maximum height reached are determined by the initial conditions and the coefficient of restitution. When $e < 1$, the motion results in an infinite accumulation of impacts within a finite time, a phenomenon known as Zeno’s paradox. In this section, we compare the displacement time histories obtained using the semi-explicit NSN scheme with the analytical solution and the two alternative nonsmooth time-integration schemes, for both elastic ($e = 1$) and inelastic ($e < 1$) collisions. Although the ball is a scalar SDOF system, we present the schemes in their general matrix–vector form to maintain consistency with the bar problem that follows.

The MJ scheme with $\theta = \frac{1}{2}$ is an implicit time-integration method derived by integrating the distributional form of the equations of motion (31) over the time step $[t_n, t_{n+1}]$. Displacements are updated using a midpoint rule (θ -method with $\theta = \frac{1}{2}$). Note that for any vector \mathbf{z} , the θ -interpolated value is defined as $\mathbf{z}_{n+\theta} = (1 - \theta)\mathbf{z}_n + \theta\mathbf{z}_{n+1}$. The general case for any value of θ leads to the following set of equations:

$$\begin{cases} \mathbf{M}(\mathbf{v}_{n+1} - \mathbf{v}_n) + \Delta t \mathbf{K} \mathbf{u}_{n+\theta} = \Delta t \mathbf{f}_{n+\theta}^{\text{ext}} + (\mathbf{H}^{\mathcal{A}})^{\top} \mathbf{p}_{n+1}^{\mathcal{A}}, & (54a) \\ 0 \leq \mathbf{p}_{n+1}^{\mathcal{A}} \perp \mathbf{H}^{\mathcal{A}} \mathbf{v}_{n+1} + e \mathbf{H}^{\mathcal{A}} \mathbf{v}_n \geq 0, \quad \text{with } \mathcal{A} = \left\{ i \mid g_i(\mathbf{u}_{n+1}^{\text{pred}}) \leq 0 \right\} & (54b) \\ \mathbf{u}_{n+1} = \mathbf{u}_n + \Delta t ((1 - \theta) \mathbf{v}_n + \theta \mathbf{v}_{n+1}), & (54c) \end{cases}$$

with $\mathbf{u}_{n+1}^{\text{pred}} = \mathbf{u}_n + \Delta t \mathbf{v}_n$ the predicted displacement at step $n + 1$.

While various explicit schemes for nonsmooth dynamics exist [46–48], the CDL scheme [45] was selected for its formulation within the NSCD framework. In the same spirit as NSN, the CDL scheme treats contact implicitly within an explicit scheme; however, they differ fundamentally in how the contact impulse feeds back into the displacement and velocity. From a smooth-nonsmooth split of the dynamics, NSN employs a predictor–corrector approach, that corrects both the velocity and the displacement within the same step, whereas CDL adopts a staggered half-step discretization: the contact active set \mathcal{A} is determined by the displacements at step $n + 1$, which then governs the impulse $\mathbf{p}_{n+\frac{3}{2}}$ used to update velocities for the same subsequent half-step $n + \frac{3}{2}$. In this configuration, the displacement \mathbf{u}_{n+1} remains purely explicit and uncorrected by the current contact forces. Formally, the CDL scheme is derived by integrating the distributional equations of motion (31) over the interval $\left[t_{n+\frac{1}{2}}, t_{n+\frac{3}{2}} \right]$:

$$\begin{cases} \mathbf{M} \left(\mathbf{v}_{n+\frac{3}{2}} - \mathbf{v}_{n+\frac{1}{2}} \right) + \Delta t \mathbf{K} \mathbf{u}_{n+1} = \Delta t \mathbf{f}_{n+1}^{\text{ext}} + (\mathbf{H}^{\mathcal{A}})^{\top} \mathbf{p}_{n+\frac{3}{2}}^{\mathcal{A}}, & (55a) \\ 0 \leq \mathbf{p}_{n+\frac{3}{2}}^{\mathcal{A}} \perp \mathbf{H}^{\mathcal{A}} \mathbf{v}_{n+\frac{3}{2}} + e \mathbf{H}^{\mathcal{A}} \mathbf{v}_{n+\frac{1}{2}} \geq 0, \quad \text{with } \mathcal{A} = \{ i \mid g_i(\mathbf{u}_{n+1}) \leq 0 \} & (55b) \\ \mathbf{u}_{n+1} = \mathbf{u}_n + \Delta t \mathbf{v}_{n+\frac{1}{2}} & (55c) \end{cases}$$

The CDL scheme can be understood as an adaptation of the symplectic Euler integrator to the contact setting. Introducing the half-step velocity as a staggered state variable, i.e., performing the change of variables $(\mathbf{u}_n, \mathbf{v}_n) \mapsto (\mathbf{u}_n, \mathbf{v}_{n+\frac{1}{2}})$, reveals an underlying partitioned structure: the displacement is advanced explicitly through $\mathbf{u}_{n+1} = \mathbf{u}_n + \Delta t \mathbf{v}_{n+\frac{1}{2}}$, while the implicit coupling is confined entirely to the velocity and contact force updates at the subsequent half-step. This staggering is geometrically motivated: contact detection occurs at the integer instant t_{n+1} via \mathbf{u}_{n+1} , and the nonsmooth velocity jump is localized naturally between the pre-impact velocity $\mathbf{v}_{n+\frac{1}{2}}$ and the post-impact velocity $\mathbf{v}_{n+\frac{3}{2}}$. Because the kinematic advance remains uncoupled from the current contact impulse, the active set is evaluated at the exact updated configuration, and the contact LCP retains a particularly efficient, decoupled structure.

In contrast, the NSN scheme employs a predictor-corrector approach. By using a smooth predictor $\tilde{\mathbf{u}}_{n+1}$ to detect potential contact, the algorithm can solve for a corrective velocity $\hat{\mathbf{v}}_{n+1}$. It enables simultaneous updates of velocities and displacements in a single step. While the NSN corrector pulls \mathbf{u}_{n+1} toward the feasible domain, small residual penetrations may persist because the correction is linearized at the velocity level. Conversely, the CDL scheme does not correct \mathbf{u}_{n+1} : the integer-step displacement remains purely explicit, and any overlap with the obstacle is resolved only in the subsequent half-step through the velocity jump. The distinction between these two strategies—staggered in CDL versus predictor-corrector in NSN—is illustrated for a bouncing ball problem in Figure 3.

To be consistent with the simulation parameters of Di Stasio et al. [49], the mass of the ball is set to $m = 1$ kg, the initial height to $u_0 = 1$ m, and the gravitational acceleration to $g = 9.81$ m/s². Simulations are run for a total time of $T = 5$ s, with a time step set initially to $\Delta t = 10^{-2}$ s. The displacement time histories, as well as their deviation from the analytical solution $u - u_a$, are presented in Figure 4 for both elastic ($e = 1$) and inelastic ($e = 0.8$) collisions.

All three schemes accurately capture the bouncing-ball dynamics, exhibiting only small shifts due to the lower-order accuracy at contact times. For both elastic and dissipative contacts, the NSN scheme matches the results of the MJ scheme exactly. This equivalence occurs when, under constant acceleration, the trapezoidal integration in MJ becomes algebraically equivalent to the central-difference integration in NSN—both during free flight and at the impact step, where acceleration terms cancel out. Provided that contact detection happens simultaneously, both schemes yield identical updates (see Appendix B for further details). Additionally, under these specific initial conditions and time-step choice, the CDL scheme exhibits a slight phase shift relative to the other two schemes, as shown in the error plot and consistent with observations in [49]. For these two test cases, the NSN scheme achieves accuracy comparable to, or better than, that of the two established nonsmooth contact dynamics schemes studied here.

For a more systematic study, we examine the effect of time-step refinement on the accuracy of the schemes by performing a convergence study for both $e = 1$ and $e = 0.8$. Approximately 50 time step values ranging from $\Delta t = 10^{-6}$ s to $\Delta t = 10^{-1}$ s on a log scale are considered. The error in displacement η is computed using the following normalized L^1 norm [45, 49, 50]:

$$\eta = \frac{\sum_{i=1}^N \|u_i - u_a(t_i)\|}{\sum_{i=1}^N \|u_a(t_i)\|}, \quad (56)$$

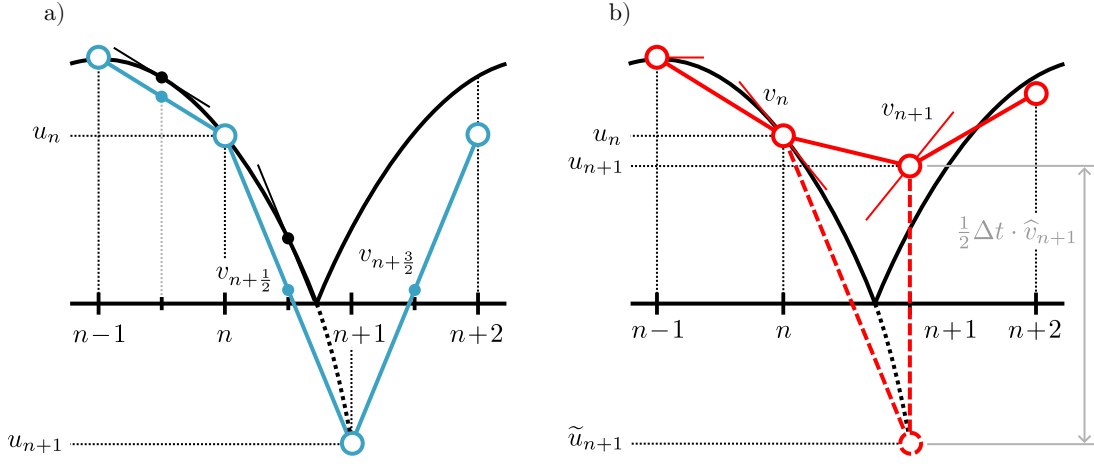


Figure 3: Schematic comparison of the time discretization and contact update logic of CDL (left) and NSN (right). In both **a)** and **b)**, the solid black line represents the analytical solution $u(t)$. The outlined circles represent the positions at full steps, and velocities are shown as slopes. In **a)**, the staggered structure of the CDL scheme is presented, with small blue circles representing when the velocities are evaluated, at half-steps. The CDL scheme detects contact at t_{n+1} and corrects the velocity at $t_{n+\frac{3}{2}}$, using the impact law that relates $v_{n+\frac{3}{2}}$ to $v_{n+\frac{1}{2}}$. **b)** The NSN scheme employs a predictor-corrector approach. If the smooth displacement update \tilde{u}_{n+1} violates the contact constraint (dashed outlined circle), a velocity correction \hat{v}_{n+1} based on the impact law, is used to correct simultaneously the velocity v_{n+1} and displacement u_{n+1} at the same step contact is detected.

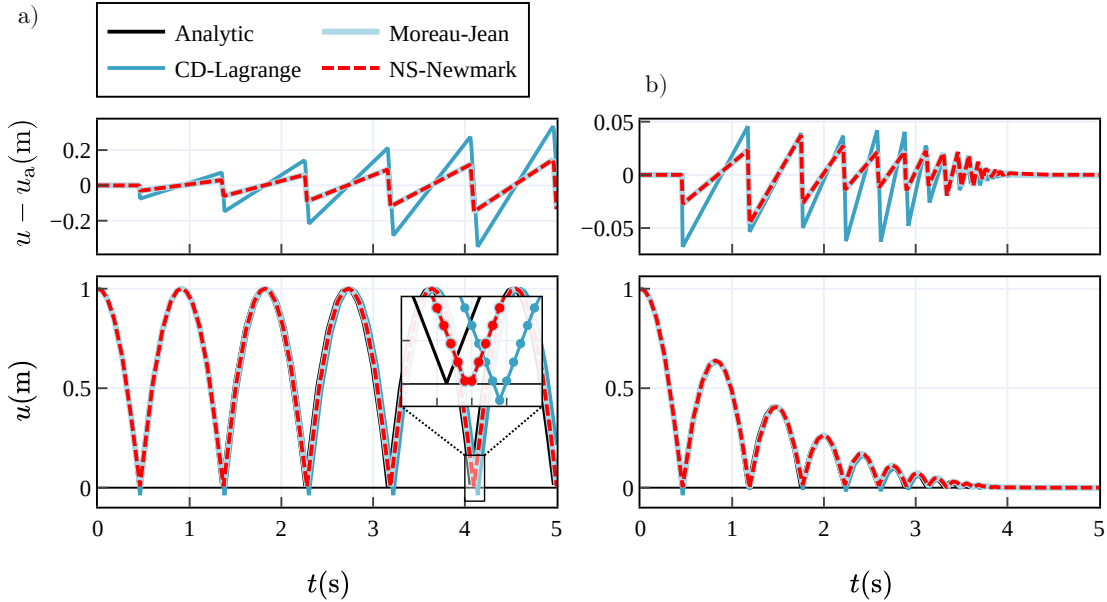


Figure 4: Comparison of displacement u and distance to the analytical solution $u - u_a$ time histories for the implicit Moreau-Jean scheme, the semi-explicit CD-Lagrange scheme, and the semi-explicit NSN scheme, for a coefficient of restitution of **a)** $e = 1$ and **b)** $e = 0.8$. Both NSN and MJ yield identical updates and a slightly better accuracy than the CDL scheme.

where u_i is the numerical displacement at step i , $u_a(t_i)$ is the analytical displacement at time t_i , and N is the total number of time steps in the simulation. Figure 5 shows the convergence of the displacement error η with respect to the time step Δt for the three schemes and two restitution coefficients. For $e = 1$ and $e = 0.8$, the schemes exhibit a convergence rate of $\eta \propto \mathcal{O}(\Delta t)$. This first-order convergence is consistent with previous studies on nonsmooth contact dynamics schemes and is explained by the first-order accuracy of impact events. For that specific test case where gravity is constant, both the MJ and NSN schemes achieve similar accuracy, with slightly lower errors than the CDL scheme across the range of time steps considered.

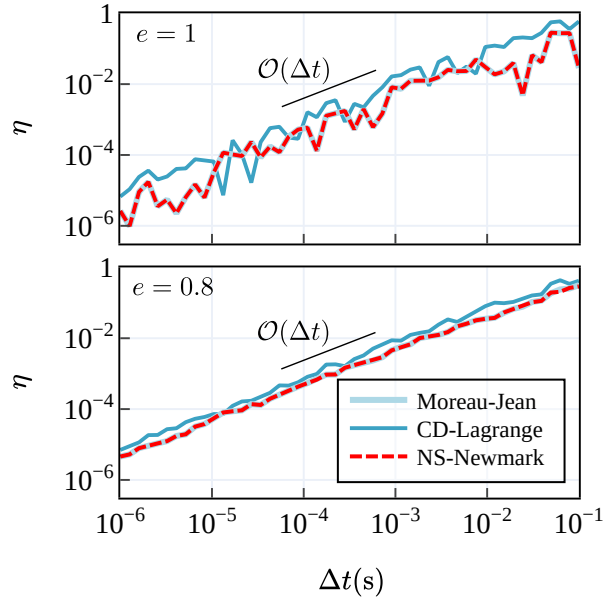


Figure 5: Comparison of the convergence rate of the error in displacement η for the implicit Moreau-Jean scheme, the semi-explicit CDL scheme, and the semi-explicit NSN scheme, for coefficients of restitution of $e = 1.0$ and $e = 0.8$. Both the MJ and NSN schemes achieve similar accuracy, with slightly lower errors than the CDL scheme across the range of time steps considered.

3.2 Impacting bar

While the previous rigid-body simulation serves as a fundamental test of the algorithm’s ability to capture impact and restitution phenomena, it does not fully exploit the second-order accuracy of the two semi-explicit schemes during free-flight phases. We therefore consider a second benchmark problem, the impacting bar, which simulates the impact of a multi-degree-of-freedom system on a rigid wall. We adopt the benchmark parameters from [45, 46, 49]: a bar of length $L = 0.254$ m, cross-sectional $A = 6.45 \cdot 10^{-4}$ m², Young’s modulus $E = 211$ GPa and density $\rho = 7847$ kg/m³. The bar is launched with an initial velocity $v_0 = 5$ m/s, with contact occurring at a single node whose position and velocity are denoted by u_c and v_c .

We discretize the bar into $N_e = 50$ P1 elements of uniform size with a time step of $\Delta t = 0.7 \times \Delta t_c \approx 6.874 \cdot 10^{-7}$ s, with Δt_c the Courant-Friedrichs-Lewy (CFL) condition. To better align with the analytical solution and eliminate non-physical oscillations immediately following the first impact, and to match results of [49], the coefficient of restitution is set to $e = 0$. This choice results in local dissipation of kinetic energy at the contact node. Results are validated against the analytical solution, which predicts a bouncing time of $t_b = 2 \times L/c$, where $c = \sqrt{E/\rho}$ is the wave speed of the bar. In the subsequent plots, we normalize position, velocity, and contact force by L , v_0 , and $F_0 = \rho \cdot c \cdot v_0 \cdot A$, respectively, while time is normalized by the bouncing time t_b . Results are shown in Figure 6.

At the chosen time step, all three schemes accurately capture the system physics, closely matching the analytical bouncing time and the characteristic rectangular contact-force profile. However, a closer inspection of the transition phases reveals subtle numerical distinctions:

- At the initial impact ($t/t_b = 0$), the contact force shows slightly larger oscillations for the NSN scheme compared to the others. These oscillations tend to be rapidly damped out.
- At the contact release ($t/t_b = 1$), the inset in the position plot reveals a close match between the two second-order schemes (NSN and CDL), with a slight advantage for CDL, while the MJ scheme shows a slight shift. Additionally, at this time, the NSN scheme exhibits the lowest residual oscillations in the velocity.

To further investigate the accuracy of the schemes, we perform a convergence study by refining the mesh and the time step simultaneously ($N_e \in [1, 5 \cdot 10^3]$, $\Delta t = 0.999 \Delta t_c$). The L^1 errors (56) for displacement, η_u , and velocity, η_v , are computed with respect to the analytical solution after contact release ($t/t_b > 1$) for a duration of $t = 3t_b$. While $e = 0$ provides a clean comparison by dissipating energy at the contact node, we also evaluate the perfectly elastic limit ($e = 1$). Testing $e = 1$ allows us to observe how the schemes handle frequent discrete velocity jumps at the contact interface in the absence of contact dissipation. By examining both the $e = 0$ and $e = 1$ cases, we verify the robustness of the convergence rates across the full range of impact physics. The results are shown in Figure 7.

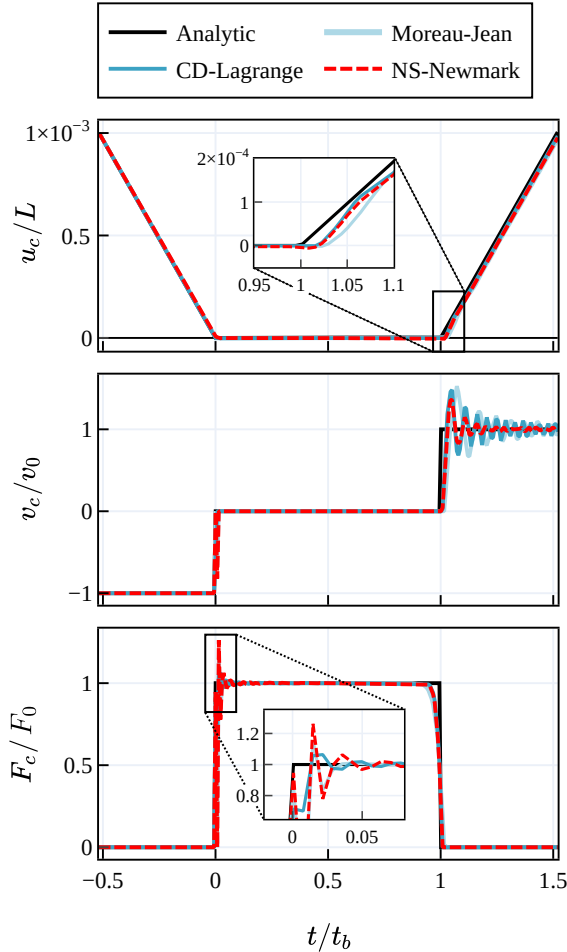


Figure 6: Comparison of semi-explicit NSN, semi-explicit CDL and implicit MJ schemes with the 1D elastic bar impact analytical solution. The results show the normalized contact node position (u_c/L) (top), velocity (v_c/v_0) (middle), and contact force (F_c/F_0) (bottom) over the normalized bouncing time t/t_b . All simulations use $N = 50$ elements and a restitution coefficient of $e = 0$.

The convergence results indicate that non-constant acceleration significantly alters the performance of the numerical schemes, favoring second-order schemes in free flight. For the perfectly plastic case ($e = 0$), both NSN and CDL maintain a robust convergence rate of $\mathcal{O}(\Delta t)$ for both displacement and velocity. Their error magnitudes are nearly identical, yielding a significant efficiency gain over the MJ scheme, which degrades at $\mathcal{O}(\Delta t^{0.5})$ across all tested configurations. Evaluating the perfectly elastic limit ($e = 1$) reveals critical differences. Without dissipation at the contact node to stabilize the interface, the velocity convergence rate (η_v) for both NSN and CDL degrades to $\mathcal{O}(\Delta t^{0.5})$. However, they successfully maintain $\mathcal{O}(\Delta t)$ for displacement (η_u). More importantly, while their asymptotic rates are similar in this limit, the absolute error magnitudes diverge significantly: the NSN scheme yields substantially lower errors than CDL across the tested time steps. This result underscores the advantage of the simultaneous predictor-corrector approach used in NSN, which proves more robust than the staggered update logic of CDL when handling the repeated velocity jumps at the contact interface.

Taken together, these benchmark results indicate that the NSN scheme is a reliable formulation capable of handling a broad spectrum of contact dynamics, from isolated rigid-body collisions to the sustained contact interactions found in elastic systems. Having established its theoretical and practical standing among nonsmooth integrators, we next evaluate the semi-explicit NSN scheme in a scenario representative of dynamic fragmentation. It compares its performance with traditional penalty-based formulations for contact.

3.3 Impacting bar with internal damage

In fragmentation scenarios, where interactions between crack faces and multiple fragments are omnipresent, traditional penalty-based formulations are preferred for their computational efficiency. In these methods, penetration is resisted by a force proportional to the penalty stiffness ϵ_n and to the penetration magnitude. However, selecting an appropriate value

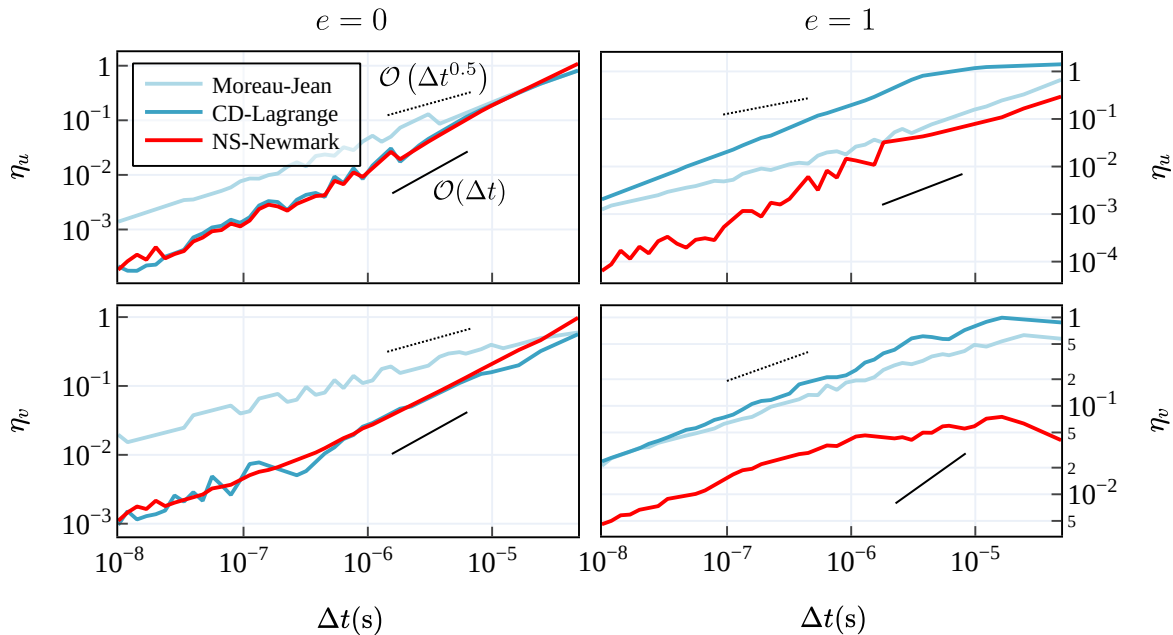


Figure 7: Time-step convergence of displacement errors η_u (top) and velocity errors η_v (bottom) for the impacting bar benchmark, comparing perfectly plastic $e = 0$ (left) and elastic $e = 1$ (right) impacts. Errors are evaluated from $t/t_b > 1$ for a duration of $t = 3t_b$, with coupled spatio-temporal refinement ($N_e \in [1, 5 \cdot 10^3]$, $\Delta t = 0.999\Delta t_c$). The MJ scheme exhibits $\mathcal{O}(\Delta t^{0.5})$ convergence in all cases. Both NSN and CDL achieve $\mathcal{O}(\Delta t)$ convergence, except for velocity at $e = 1$ where the rate drops to $\mathcal{O}(\Delta t^{0.5})$. Notably, NSN yields significantly lower error magnitudes than CDL in the purely elastic regime.

for ϵ_n necessitates a compromise between accuracy and stability. While high stiffness is required to minimize unphysical penetration, it also limits the stability to prohibitively small time steps. Additionally, as demonstrated in [30], the nonsmooth loading path induced by this artificial contact stiffness generates energy artifacts in explicit time-integration schemes. If an interface oscillates around a null gap, repeatedly entering and leaving contact, artifacts often accumulate, potentially leading to global instability in the simulation. We present the limitations of such an approach in the following study and compare it with the NSN scheme. To that end, we adapt the previous benchmark to simulate the impact of a bar with internal damage. The internal damage is modeled using cohesive elements. Theoretically, the damage affects only the material's 1D tensile behavior and should therefore not affect its compressive behavior. It is expected that the bouncing time t_b is the same as the non-damaged scenario. However, when using the penalty method for contact, we expect the contact penalty to affect the simulation's accuracy and stability, as they influence the bar's compliance under compression.

We remark that while standard Courant-Friedrichs-Lewy (CFL) conditions ($\Delta t \leq h_{\min}/c$) govern the bulk stability, they fail to account for the additional stiffness k_{add} from cohesive zones or contact penalties. These high-stiffness terms increase the system's maximum natural frequency, ω_{\max} , thereby reducing the stable time step. To ensure the numerical stability of each case, we calculate the critical time step using a conservative estimate based on Gershgorin's circle theorem [51]. Using a lumped mass matrix \mathbf{M} , Gershgorin's theorem bounds the maximum eigenvalue of $\mathbf{M}^{-1}\mathbf{K}$, $\lambda_{\max} = \omega_{\max}^2$ by the maximum row sum of the stiffness matrix scaled by the nodal mass:

$$\omega_{\max}^2 \leq \max_i \left(\frac{\sum_j |\mathbf{K}_{ij}^{\text{bulk}}|}{\mathbf{M}_{ii}} + \frac{k_{\text{add}}}{\mathbf{M}_{ii}} \right) \approx \omega_{\text{bulk}}^2 + \omega_{\text{add}}^2 \quad (57)$$

We compute the stable time step using the updated ω_{\max} , $\Delta t \leq 2/\omega_{\max}$, thereby ensuring theoretical stability. In practice, additional safety factors are necessary to account for nonsmooth loading paths, further reducing the permissible Δt . Note that in one dimension and with $k_{\text{add}} = 0$, this bound gives exactly the standard CFL condition.

To fit the subsequent simulations, the bar has a length of $L = 10^{-3}$ m and is made of AD-995 alumina, with material properties listed in Table 1. It is discretized with $N_e = 2 \cdot 10^3$ P1 elements. To model high levels of internal damage, $N_{\text{coh}} = 10^3$ cohesive elements, whose damage is initialized at $d_0 = 10^{-3}$, are inserted into the mesh. This damage level yields a cohesive stiffness $k(d_0)$ (Eq. 19) smaller than the characteristic stiffness of a bulk element E/h_e , with $h_e = L/N_e$, ensuring the convexity of the contact problem is not influenced by cohesion. For the penalty-based comparison, we define a contact penalty $\epsilon_n = \alpha E/h_e$ with $\alpha \in [10^{-2}, 10^2]$.

Parameter	Value
Young's modulus, E [GPa]	370
Density, ρ [kg/m ³]	3900
Cohesive strength σ_c [MPa]	262
Fracture toughness, G_c [J/m ²]	50

Table 1: AD-995 alumina material parameters.

Displacement and velocity time evolution and convergence. Figure 8 shows the results of the bouncing bar (with internal damage), in terms of displacement and velocity of the contact node (u_c, v_c), and the corresponding L^2 errors. The specific displacements and velocity of Fig. 8b-c are indicated on Fig. 8d-e as black outlined markers. As evidenced in Fig. 8b, the penalty method exhibits strong sensitivity to the normalized contact stiffness, α . Low stiffness values lead to significant unphysical penetration and delayed rebound, thereby failing to capture the kinematics accurately. Conversely, increasing the stiffness to enforce non-penetration better introduces high-frequency oscillations in the velocity field (Fig. 8c). It also severely restricts the stability region (Fig. 8d-e, vertical dashed lines). For an acceptable error on position, the penalty method ideally requires $\alpha \geq 10^2$, which is stable from $\Delta t/\Delta t_{c,\text{bulk}} \approx 5 \cdot 10^{-2}$. In contrast, the nonsmooth solution (red line) enforces the contact condition without tuning a penalty parameter, maintaining low, stable errors in both position and velocity over a wide range of time steps. It achieves displacement accuracy comparable to the penalty method at $\alpha \approx 10^2$ and significantly lower velocity errors, even with $\Delta t/\Delta t_{c,\text{bulk}} \approx 1$.

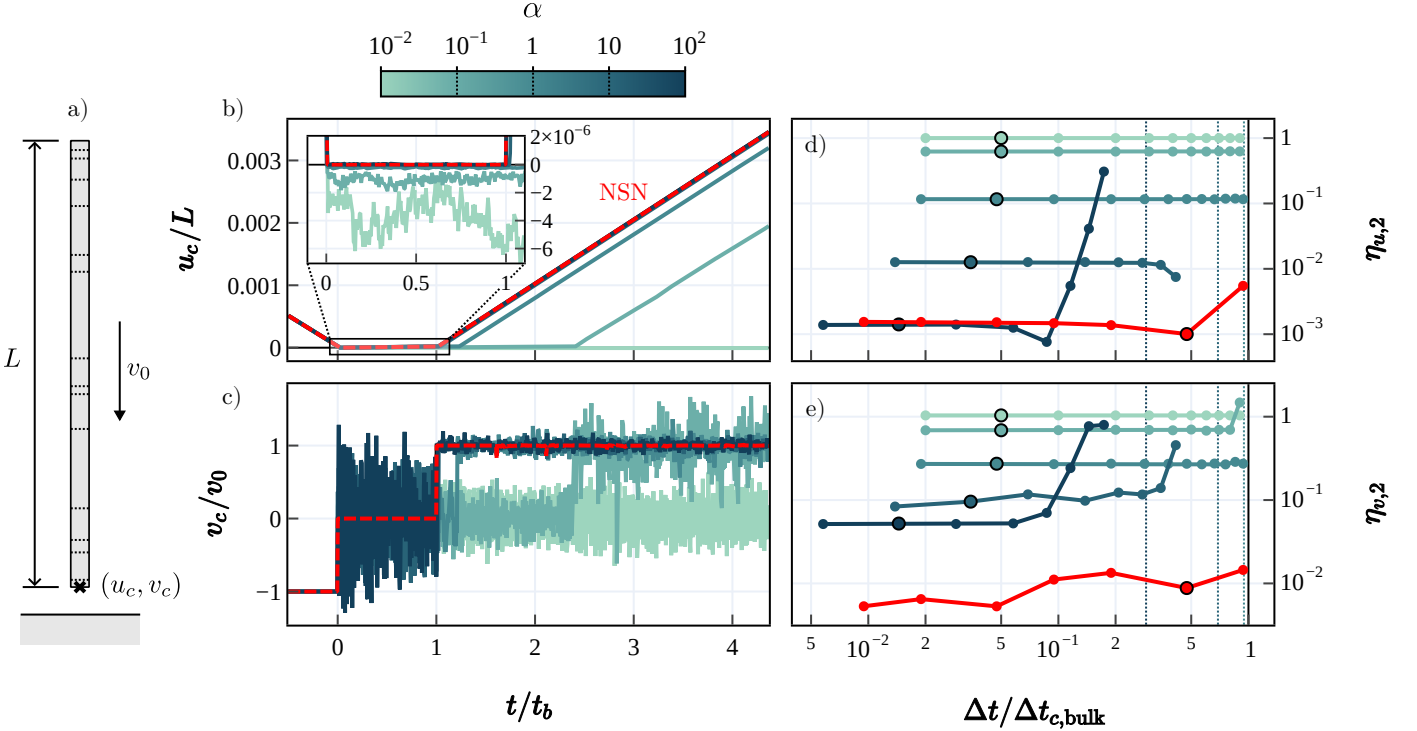


Figure 8: **(a)** Schematic of a bar of length L and material properties E, ρ , discretized with $N = 2 \cdot 10^3$ P1 elements, with $N_{\text{coh}} = 10^3$ inserted cohesive elements (dashed lines) of properties σ_c, G_c, d , to represent a highly damaged bar, launched against a rigid obstacle with a rigid-body velocity of v_0 . Comparison of the contact node position u_c **(b)** and velocity v_c **(c)** with respect to time t/t_b for the penalty-based method with different normalized penalty values $\epsilon_n = \epsilon_n/(E/\bar{h}_e)$, compared to the nonsmooth solution (red line). Figure **(d)** and **(e)** show the L^2 norm of the error in the contact node position and velocity against the analytical solution after impact, as a function of the normalized time step $\Delta t/\Delta t_{c,\text{bulk}}$. $\Delta t_{c,\text{bulk}}$ represents the stable time step of the bulk elements without the additional stiffness contribution of contact or cohesion. The corresponding stable time steps, accounting for additional stiffness, are shown as dashed lines. The red line indicates the error for the nonsmooth solution. Specific time evolution of displacement and velocity from **(b)**-**(c)** is indicated with black outlined markers on **(d)**-**(e)**.

Energy conservation and computational cost. While the explicit Newmark- β scheme only conserves the total mechanical energy \mathcal{E} in a weak sense (oscillating around the mean), it conserves the algorithmic energy \mathcal{H} exactly for a

smooth evolution of the system. This quantity augments the mechanical energy with an acceleration-dependent term [52, 53]:

$$\mathcal{H} = \underbrace{\frac{1}{2} \mathbf{v}^\top \mathbf{M} \mathbf{v} + \frac{1}{2} \mathbf{u}^\top \mathbf{K} \mathbf{u}}_{\mathcal{E}} - \frac{\Delta t^2}{8} \mathbf{a}^\top \mathbf{M} \mathbf{a} \quad (58)$$

As proven in [53], NSN guarantees this conservation in the presence of contact as well, provided they are non-dissipative. Otherwise, dissipation is controlled by the coefficient of restitution e . This theoretical property is numerically verified in Figure 9. The left panel plots the maximum relative error $\Delta\mathcal{H}/\mathcal{H}_0$ against the normalized time step. The NSN method (red line) exhibits a flat error profile hovering around 10^{-12} , independent of the time step. This value can be attributed to the accumulation of errors of the order of 10^{-14} , the set tolerance of the contact solver. In contrast, the penalty-based method exhibits energy errors that converge to a plateau between 10^{-5} and 10^{-7} for small time steps, with lower accuracy for larger penalty values. The right panel of Figure 9 translates this into a practical efficiency metric: energy error versus total CPU time. All the simulations were run on an Intel(R) Xeon(R) Platinum 8360Y CPU @ 2.40 GHz. While the implicit nature of the NSN contact solver increases per-step costs by a factor of ~ 5 , its robustness permits significantly larger time steps, leading to a faster total time-to-solution. This efficiency is achieved without compromising accuracy; in fact, NSN yields an energy-conservation error nearly seven orders of magnitude lower than that of the stiffest penalty-based approach tested, while achieving a CPU time roughly 27 times smaller. By decoupling physical accuracy from the time-step constraints inherent to penalty methods, the nonsmooth approach effectively bypasses the traditional trade-off between contact stiffness and computational cost, enabling high-fidelity long-term simulations.

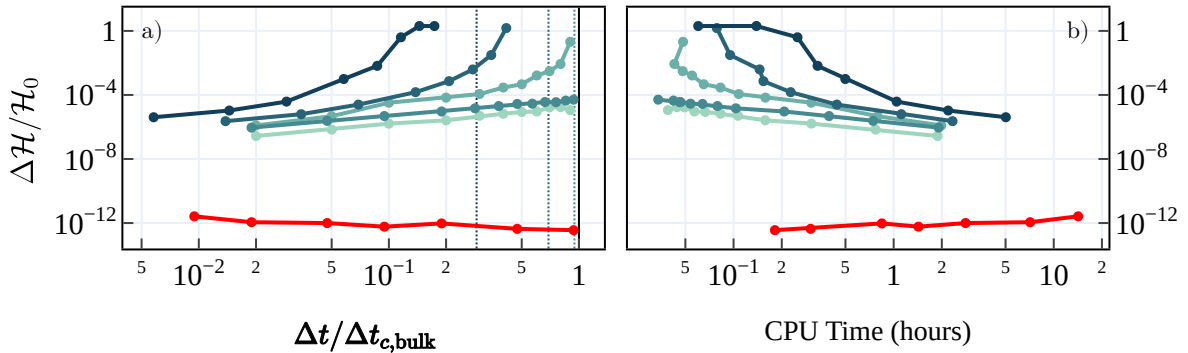


Figure 9: **(a)** Convergence analysis of the relative algorithmic energy error $\Delta\mathcal{H}/\mathcal{H}_0$ as a function of the normalized time step $\Delta t/\Delta t_{c,bulk}$. The nonsmooth solution (red line) maintains energy conservation at machine-precision levels ($\approx 10^{-12}$), effectively independent of the time-step size. In contrast, the standard penalty-based schemes (blue lines) exhibit a characteristic convergence order, with accuracy degrading as Δt increases, eventually diverging near their respective stability limits (vertical dashed lines). **(b)** Computational efficiency assessment plotting the energy error against the total CPU time. Although the semi-implicit nature of the nonsmooth formulation incurs a computational cost approximately 5 times higher per time step, its unconditional energy stability allows the use of significantly larger time steps, resulting in a lower total time-to-solution for high-precision results compared to the penalty-based method.

4 Application to dynamic fragmentation

In this section, we apply the proposed contact algorithm to simulate the dynamic fragmentation of an expanding ring. This benchmark problem is widely used to validate fracture and fragmentation models because of its well-characterized behavior at high strain rates. We first present the standard free expansion ring fragmentation, and then detail a modified version that introduces walls to confine the process and increase contact interactions. To the best of our knowledge, fragment statistics in an expanding-ring configuration with rigid walls that confine the expansion and intensify fragment–fragment and fragment–wall interactions have not been systematically examined in the literature. This modified setup, therefore, provides a contact-rich benchmark for assessing the robustness of the proposed contact algorithm and yields interesting physics.

4.1 Free expanding ring fragmentation

The Mott ring is a circular ring of radius r subjected to rapid uniform radial expansion, driven by high internal pressure p_{int} , which induces high strain rates and eventual fragmentation due to tensile failure (Figure 10a). While the failure is driven by tension, contact mechanics play a critical role in the post-fracture regime. Once fragmentation begins, the sudden

release of stress generates compressive waves that trigger contact between the newly created cohesive surfaces. Secondary collisions between fragments may also occur. To capture this process numerically, we employ the extrinsic cohesive zone framework implemented in the open-source software **Akantu** [26], coupled with a custom Python implementation of the NSN scheme.

4.1.1 Problem setup

We study the one-dimensional equivalent of this system: a bar with length L , centered at the origin along the x -axis. To simulate the expansion of the ring, the bar is initialized with a velocity field $v(x) = \dot{\epsilon}x$, where $\dot{\epsilon}$ is the imposed constant strain rate (Figure 10b). The boundaries of the bar are displaced with a velocity of $\pm\dot{\epsilon}L/2$ to ensure uniform expansion, then released once fragmentation occurs. The material is modeled using the AD-995 alumina parameters listed in Table 1.

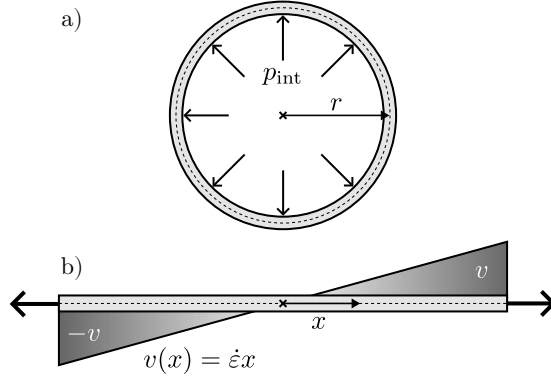


Figure 10: Schematic of the expanding ring fragmentation benchmark. The circular ring of radius r under strong internal pressure p_{int} (a) is modeled by a one-dimensional equivalent bar centered at $x = 0$ (b) with an initial velocity field $v(x) = \dot{\epsilon}x$ to simulate the expansion. The boundaries of the bar are pulled at a velocity $\pm\dot{\epsilon}L/2$ until fragmentation starts.

Following Camacho and Ortiz (1996), and Drugan (2001) [20, 54], we define the characteristic scales of the problem based on the material's elastic properties (E , ρ) and cohesive law properties (σ_c , G_c). First, the longitudinal wave speed is defined as $c = \sqrt{E/\rho}$. From the energy per unit area required to reach full decohesion (fracture energy G_c), we derive the characteristic material time t_0 :

$$t_0 = \frac{EG_c}{\sigma_c^2 c}. \quad (59)$$

This timescale physically represents the duration of the cohesive fracture process, i.e., the time required for a cohesive interface to evolve from intact to fully separated under stresses on the order of σ_c transmitted by longitudinal waves. The characteristic material length $s_0 = ct_0$ represents the distance a stress wave travels during the total decohesion process [55]. Finally, we introduce the characteristic strain rate $\dot{\epsilon}_0$ as the strain rate at which the elastic strain reaches the fracture deformation threshold (σ_c/E) over the characteristic time t_0 :

$$\dot{\epsilon}_0 = \frac{\sigma_c}{Et_0}. \quad (60)$$

These scales allow us to express the imposed strain rate, the resulting fragment sizes, and the fracture energy in non-dimensional forms: $\hat{\epsilon} = \dot{\epsilon}/\dot{\epsilon}_0$, $\hat{s} = s/s_0$, and $\hat{\mathcal{G}} = \mathcal{G}/G_c$ respectively. The transition from quasi-static to dynamic regime occurs at $\hat{\epsilon} \approx 1$.

4.1.2 Energy budget

In this dynamic regime described by Grady's model [44], fragmentation is governed by a local energy budget. As the bar of length L expands at a constant strain rate $\dot{\epsilon}$, the average fragment size s emerges from a balance between the local kinetic energy and the fracture energy G_c . For a single fragment i of size s , the local kinetic energy density is calculated by integrating the energy density over the fragment domain $[-s/2, s/2]$:

$$\mathcal{K}_{\text{local},i} = \int_{-s/2}^{s/2} \frac{1}{2} \rho (\dot{\epsilon}x)^2 dx = \frac{\rho \dot{\epsilon}^2 s^3}{24}. \quad (61)$$

A fragment is formed when this available local kinetic energy is sufficient to overcome the material's resistance to fracture, defined by the fracture energy G_c . By equating the source ($\mathcal{K}_{\text{local},i}$) to the sink (G_c), the characteristic fragment size for

free expansion is given by:

$$\bar{s}_{\text{free}} = \left(\frac{24G_c}{\rho\dot{\epsilon}^2} \right)^{1/3}, \quad (62)$$

with a fragment size scaling with the strain rate as $s \propto \dot{\epsilon}^{-2/3}$. In this regime, Grady assumes that only kinetic energy is available to drive fragmentation and that all fragments have the same size. For lower strain rates, the elastic energy stored in the bar makes a significant contribution to the energy budget. Glenn and Chudnovsky [56] extended Grady’s model to account for this energy contribution, which becomes dominant when ($\hat{\epsilon} < 1$), resulting in a model accounting for two distinct regimes: quasi-static and dynamic. Later, Zhou et al. [55] proposed a model fitted to numerical results from a cohesive zone model that integrates the effects of wave propagation, contact, and damage evolution. The three normalized fragment size predictions from these models are given by:

$$\hat{s}_{\text{Grady}} = \frac{\bar{s}_{\text{free}}}{s_0} = \left(\frac{24}{\hat{\epsilon}^2} \right)^{1/3}, \quad \hat{s}_{\text{G\&C}} = \frac{4}{\hat{\epsilon}} \sinh \left[\frac{1}{3} \sinh^{-1} \left(\frac{3}{2} \hat{\epsilon} \right) \right], \quad \hat{s}_{\text{ZMR}} = \frac{4.5}{1 + 4.5\hat{\epsilon}^2/3}. \quad (63)$$

ZMR model deviates from G. & C. at low strain rates by predicting larger fragments. Although Glenn and Chudnovsky’s model assumes that all the elastic energy is converted into fracture energy, the ZMR model accounts for the fact that the fragmentation is not instantaneous and that almost half of the elastic energy is kept as residual kinetic energy in the form of wave propagation, i.e., vibration of the fragments. At higher strain rates, the ZMR model predicts the same $s \propto \dot{\epsilon}^{-2/3}$ scaling but with smaller fragments than both Grady and G. & C. models, in closer agreement with experimental observations. In that regime, the system extracts more kinetic energy from the bar’s global motion, notably due to contact interactions. To verify the ability of the proposed NSN scheme to capture these contact interactions and their influence on fragmentation, we perform simulations for a wide range of such non-dimensional strain rates, specifically $\hat{\epsilon} \in [10^{-3}, 10^3]$, covering the quasi-static and dynamic range.

4.1.3 Numerical implementation

We conduct simulations of the expanding ring benchmark using both the penalty-based contact method and the proposed NSN scheme. The mesh choices are detailed in Appendix C, following the recommendations of [24, 57, 58] for converged numerical results. For the penalty-based approach, we select a penalty stiffness of $\epsilon_n = 10E/\bar{h}_e$, with \bar{h}_e the mean element length of the mesh, and the regular Camacho-Ortiz TSL with no capping. NSN uses a coefficient of restitution $e = 1$, representing perfectly elastic collisions, and the modified TSL introduced in Section 2.4. The stiffness cap for cohesive elements is set to $\tilde{k} = 10E/\bar{h}_e$, such that the two contact approaches share the same maximum stiffness, one for contact and the other for cohesion, thereby defining the same maximum stable time step Δt_c (Section 3.3). The actual time step is set to $\Delta t = 0.2\Delta t_c$ for the penalty-based method to ensure stability and $\Delta t = 0.99\Delta t_c$ for the nonsmooth method. The results are compared against the predictions from Grady [44], Glenn and Chudnovsky (G. & C.) [56], and Zhou et al. (ZMR) [55].

While the first two models (Grady and G. & C.) provide theoretical predictions for both fragment size and fracture energy, the ZMR model provides a closed-form prediction for fragment size only, fitted on numerical simulations. We approximate the fracture energy for the ZMR model as $\hat{\mathcal{G}}_{\text{ZMR}} = 1/\hat{s}_{\text{ZMR}}$, which represents the theoretical surface energy required to create fragments of size \hat{s}_{ZMR} . However, this approximation assumes that all energy is dissipated through fracture, neglecting the internal damage mechanisms present in the CZM simulations of [55]. Therefore, $\hat{\mathcal{G}}_{\text{ZMR}}$ is shown as a theoretical lower bound.

4.1.4 Results and discussion

Figure 11 presents both the average fragment size \hat{s} and the fracture energy $\hat{\mathcal{G}}$ as a function of the imposed strain rate $\hat{\epsilon}$. For a consistent comparison, the dissipated energy was normalized by the bar length, such that we plot the fracture energy per unit length. We see in Figure 11a that both contact methods yield fragment sizes that closely align with the ZMR predictions across the entire range of strain rates. At the lowest strain rate $\hat{\epsilon} = 10^{-3}$, we observe a slight deviation: the nonsmooth method yields larger fragment sizes than the penalty-based approach. This discrepancy stems from the modified TSL used in the NSN scheme. As discussed in Section 2.4, cohesive elements with low damage levels operate within the constant-traction regime of the modified law, thereby making the initial decohesion stages more energy-consuming. Given that both methods yield comparable fracture energies at this strain rate (Figure 11b), the results confirm that the modified TSL initially requires more energy to damage cohesive elements, ultimately slowing fragment formation. It underscores how the choice of traction-separation law influences fragmentation outcomes. As the strain rate increases, the damage levels in the cohesive elements rise, and the behavior converges to that of the standard linear TSL, resulting in consistent fragment sizes between the two methods. We observe in Figure 11b that both contact methods yield fracture energies that align in trend but exceed the ZMR lower bound, indicating that some energy is dissipated as diffuse damage ($d < 1$) that does not necessarily lead to fragment formation.

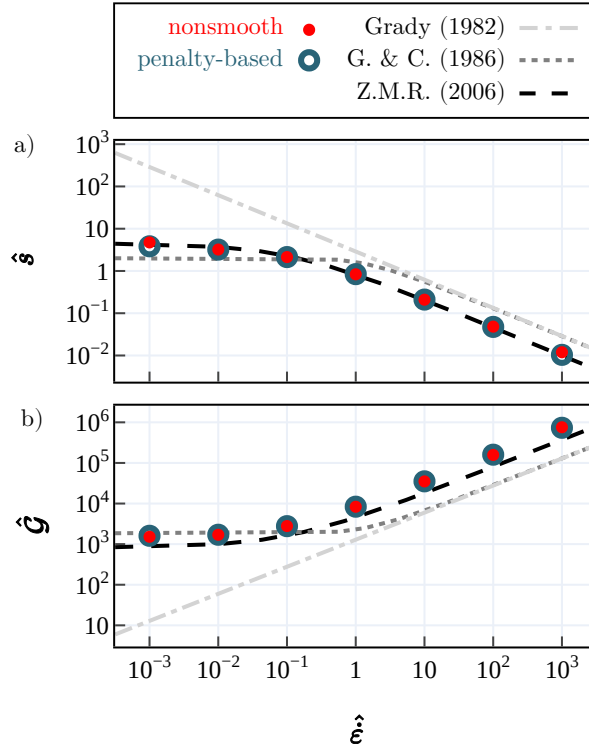


Figure 11: Comparison of fragmentation metrics for the expanding ring test. **a)** Average non-dimensional fragment size \hat{s} as a function of the imposed non-dimensional strain rate $\hat{\epsilon}$. **b)** Non-dimensional fracture energy $\hat{\mathcal{G}}$ as a function of the imposed non-dimensional strain rate $\hat{\epsilon}$. The results for both penalty-based and nonsmooth contact methods are compared against theoretical predictions from Grady [44], Glenn and Chudnovsky [56], and the ZMR model [55]. Both methods yield similar fragmentation behavior across the range of strain rates, with fragment sizes closely aligning with the ZMR predictions. A slight deviation at the lowest strain rate of the nonsmooth method is attributed to its modified traction-separation law. The fracture energy results indicate that both methods dissipate more energy than the ZMR lower bound, indicating the presence of cohesive elements with damage levels smaller than 1.

As stated in Section 3.3, the NSN approach improves the overall stability of the simulation and allows the use of larger time steps, which offsets its computational overhead. In Figure 12, we present the final number of fragments and the evolution of the algorithmic energy (58) obtained for both contact methods as a function of the time step, for a strain rate of $\hat{\epsilon} = 1$. While the nonsmooth method remains theoretically stable up to Δt_c , the penalty-based approach requires additional safety factors. We observe for the penalty-based approach that although the number of fragments is stable for time steps below $0.5\Delta t_c$, maintaining energy conservation for long simulations would require time steps at least below $0.2\Delta t_c$ for penalty-based methods. In that case, the effective overhead of the nonsmooth method would drop to a factor of 1.54. This threshold of $\Delta t < 0.2\Delta t_c$ is consistent with the results of [30], although we see it does not guarantee long-term stability.

In the next subsection, we explore a modified version of this benchmark in which the bar is confined to a box, resulting in more frequent and more intense contact interactions.

4.2 Constrained expanding ring fragmentation

This benchmark extends the previous one by introducing rigid walls that confine the bar's expansion. This modification significantly alters the fragmentation process by increasing the frequency and intensity of contact interactions. Fundamentally, the energy available for fracture switches from a local (fragment-scale) to a global (full bar-scale) energy budget.

4.2.1 Energy budget

We showed in Section 4.1.2 that in free expansion, according to Grady, each fragment pays for its own creation using only its own local kinetic energy with a fragment size proportional to the strain rate as $\bar{s}_{\text{free}} \propto \hat{\epsilon}^{-2/3}$ (62). The total dissipation $\mathcal{G}_{\text{free}} = (L/\bar{s}_{\text{free}})G_c$ results in an energy density ($\mathcal{G}_{\text{free}}/L$) that is entirely independent of the total bar length.

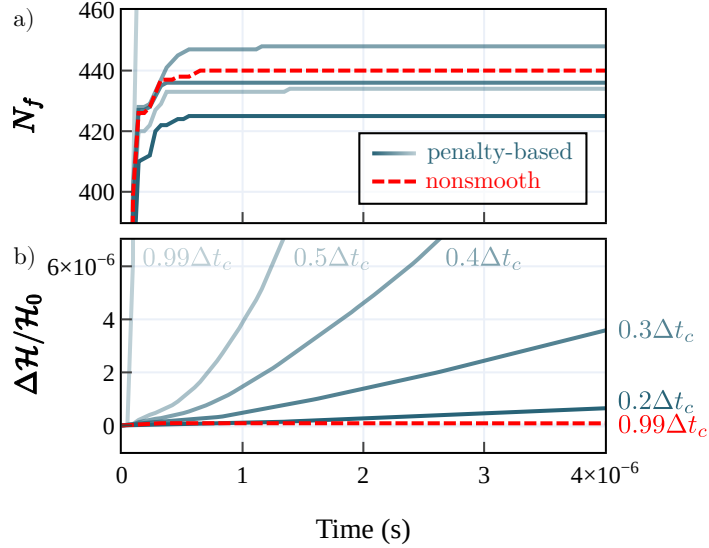


Figure 12: **a)** Sensitivity of the final fragment count to the time step size Δt for the penalty-based method ($0.2\Delta t_c \leq \Delta t \leq 0.99\Delta t_c$) compared to the nonsmooth method ($\Delta t = 0.99\Delta t_c$). **b)** Evolution of the total algorithmic energy variation over time for both methods and the varying time step sizes. The strain rate is set to $\hat{\epsilon} = 1$ for both methods, and in Figure 11, time steps were set at $0.2\Delta t_c$ and $0.99\Delta t_c$ respectively for penalty-based and nonsmooth approaches.

When the expansion is confined within boundaries, such as a rigid box, the fragments cannot simply fly away; instead, they collide with the walls and one another. These interactions effectively make the global kinetic energy, which would otherwise be lost to rigid-body motion, available to drive additional cracking. In this confined state, the energy source is no longer restricted to the local domain of a single fragment, but is instead the integral of kinetic energy across the full length L of the bar:

$$\mathcal{K}_{\text{global}} = \int_{-L/2}^{L/2} \frac{1}{2} \rho (\dot{\epsilon} x)^2 dx = \frac{\rho L^3 \dot{\epsilon}^2}{24}. \quad (64)$$

Assuming an idealized limit where all this available global energy is dissipated through the creation of N fragments, the total fracture energy $\mathcal{G}_{\text{confined}}$ must equal $\mathcal{K}_{\text{global}}$. The resulting balance, $\mathcal{K}_{\text{global}} = (L/\bar{s}_{\text{confined}})G_c$, leads to a new characteristic fragment size:

$$\bar{s}_{\text{confined}} = \frac{24G_c}{\rho L^2 \dot{\epsilon}^2}. \quad (65)$$

While the energy dissipated per unit length in free expansion is constant, the dissipated energy density in the confined case ($\mathcal{G}_{\text{confined}}/L$) scales quadratically with the bar length L^2 . The magnitude of this effect is quantified by the ratio:

$$r = \frac{\mathcal{K}_{\text{global}}}{\mathcal{K}_{\text{local}}} = \left(\frac{L}{\bar{s}_{\text{free}}} \right)^2 \quad (66)$$

This confinement forces the system to produce much smaller fragment sizes and dissipate more energy than the free-expansion baseline.

4.2.2 Numerical implementation and results

To capture this confinement behavior and evaluate these analytical limits, we employ the proposed semi-explicit NSN scheme, in which contact is treated as fully elastic, i.e., with a coefficient of restitution $e = 1$. We focus on a unit normalized strain rate ($\hat{\epsilon} = 1$) that we choose at the limit of the dynamic regime for computational reasons: with higher strain rates, the available kinetic energy for fracture increases quadratically, requiring much finer meshes and millions of time steps to achieve convergence. Ideally, this strain rate should be higher. This choice defines a fixed base fragment size \bar{s}_{free} , and we study bars of varying lengths L to explore different global-to-local energy ratios r . The box size L_{box} is calibrated to ensure that wall collisions occur after the initial free-expansion fragmentation has concluded:

$$L_{\text{box}} = L \left[1 + \alpha_{\text{box}} \left(\frac{\sigma_c}{E} + \frac{\bar{s}_{\text{free}} \dot{\epsilon}}{c} \right) \right]. \quad (67)$$

The term σ_c/E in the α_{box} product accounts for the static elastic strain required to reach the cohesive strength σ_c . The second term represents the distance the bar's edges travel during the time required for an elastic wave to propagate

through a fragment of size \bar{s}_{free} . The parameter α_{box} scales that spatial buffer. Because secondary fragmentation in this 1D benchmark arises from a sequence of spalling events, high confinement (small α_{box}) prevents it; frequent impacts keep the fragments in compression, preventing the buildup of tensile stress required for spalling. Increasing the box size provides each fragment sufficient time and space for tensile waves to develop. To ensure a sufficiently developed spalling cascade, we set $\alpha_{\text{box}} = 10^2$ for the rest of the analysis.

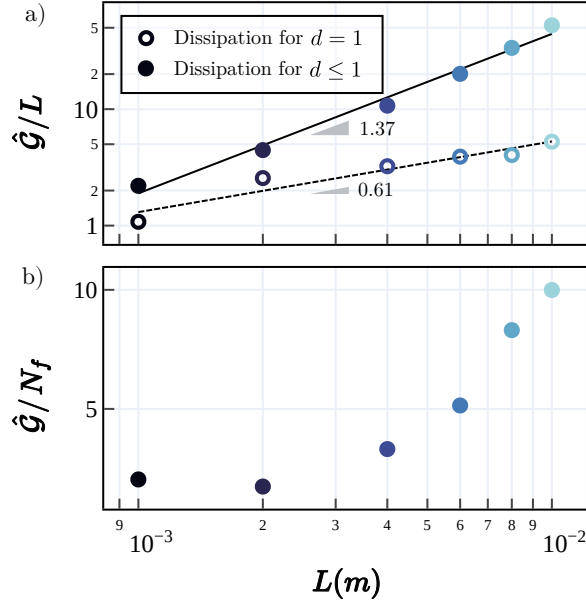


Figure 13: Effect of the domain length L on the fracture energy. **a)** Scaling of the total normalized dissipated energy ($\hat{\mathcal{G}}/L \propto L^{1.37}$) compared to the energy associated with fully formed fracture surfaces ($\propto 1/\hat{s} \propto L^{0.61}$). While the latter accounts only for fully formed cracks ($d = 1$), the total dissipation includes energy dissipated in partially damaged cohesive zones ($d < 1$). **b)** Total fracture energy $\hat{\mathcal{G}}$ normalized by the theoretical fracture energy required to create N_f fragments, $N_f \times G_c$. From both plots, we see that the increase in the bar length L leads to a significant increase in the total dissipated energy, which grows faster than the theoretical fracture energy associated with fully formed cracks. This discrepancy highlights the growing contribution of internal damage (partially damaged cohesive zones) to the overall energy dissipation as the bar length increases.

The physical limitations of idealized confined fragmentation are synthesized in Figure 13. By analyzing the scaling exponents of the different energy sinks, we can partition them and identify why the system departs from the analytical L^2 limit of energy dissipation. We distinguish three distinct types of energy allocation based on the results in Figure 13a:

- **Surface creation** ($\sim L^{0.61}$): This represents the energy strictly consumed by the creation of fully formed cracks ($d = 1$), which scales with the inverse of the mean fragment size ($\propto 1/\hat{s}$). The low exponent indicates that, as the bar length increases, the creation of new surfaces becomes a smaller fraction of the total energy dissipation.
- **Internal damage** ($\sim L^{0.61}$ to $\sim L^{1.37}$): The gap between the surface creation energy (0.61) and the total dissipated energy scaling (1.37) represents energy consumed by “internal damage”—cohesive zones that have been activated ($d > 0$) but fail to reach full separation ($d < 1$). This phenomenon is explicitly captured in Figure 13b, which plots the ratio $\hat{\mathcal{G}}/N_f$ (total energy dissipated per fully formed fragment). The fact that this ratio climbs from approximately 2 at small scales to 10 at larger scales confirms that as the bar length increases, the fragment creation process becomes less efficient.
- **Residual trapped energy** ($\sim L^{1.37}$ to $\sim L^2$): The final gap between the total dissipated energy and the theoretical limit represents the energy that the system is unable to dissipate through any fracture mechanism. This energy is retained within the fragments as rigid-body motion (kinetic energy) and internal vibrations (kinetic and strain energy). Because a stress threshold governs fragmentation, this energy remains trapped when stresses generated from impacts or internal wave reflections fail to reach the cohesive strength σ_c required to initiate or advance further fracture.

The $L^{1.37}$ scaling of energy dissipation is reasonably close compared with the expected L^2 scaling. In addition to the energy being trapped in the system rather than dissipated, the strain rate we chose at the limit of the dynamic regime, $\hat{\epsilon} = 1$, can explain the observed gap.

The results discussed thus far were obtained under the assumption of perfectly elastic contact ($e = 1$). However, the introduction of contact dissipation ($e < 1$) allows the model to account for energy lost during collisions. Leveraging the proposed NSN scheme, we explore these effects in the following section.

4.3 Effect of contact dissipation on secondary fragmentation

When using perfectly elastic contact in confined environments, once fracture saturates (i.e., no new cohesive surfaces can form), the remaining kinetic energy is conserved indefinitely. Introducing dissipative contact ($e < 1$) allows the model to dissipate energy during collisions, prompting the question of how contact dissipation affects the partitioning of energy dissipation and, consequently, secondary fragmentation. We study how the number of fragments and the energies dissipated by fracture and contact vary with the restitution coefficient $e \in [0, 1]$. The studied bar has a length $L = 5 \cdot 10^{-3}$ m, its free-expansion strain rate is set to $\dot{\epsilon} = 1$, and it is confined within a box whose size is scaled by $\alpha_{\text{box}} = 100$. Figure 14a reports the dissipated energy partition evolution, now split between fracture dissipation \mathcal{G} (dashed lines) and contact dissipation \mathcal{C} , summed with \mathcal{G} (solid lines). Both are normalized by the total injected energy,

$$\mathcal{E}_{\text{inj}} = \mathcal{E}_0 + \mathcal{W}_{\text{ext}}(t_{\text{final}}),$$

i.e., the sum of the initial energy (kinetic and strain energy) and the external work. The bottom plot shows their respective time histories, while the top one shows the final values. With contact dissipation ($e < 1$), the fracture energy \mathcal{G} drops from about 88% of \mathcal{E}_{inj} in the purely elastic case ($e = 1$) to roughly 45% for $e < 0.999$. Between $e = 0.9999$ and $e = 1$, the fracture energy increases gradually to the value of the purely elastic case. However, the total dissipated energy $\mathcal{G} + \mathcal{C}$ grows faster than in the perfectly elastic case and reaches about 98% of \mathcal{E}_{inj} over the simulated time. Remarkably, for any $e < 1$, the curves for $\mathcal{G} + \mathcal{C}$ collapse approximately onto a single evolution, suggesting that the total dissipated energy is only slightly dependent on e as soon as contact is inelastic and that contact zones are numerous.

Counterintuitively, a strong reduction in fracture dissipation does not lead to fewer fragments. As shown in Figure 14b, systems incorporating contact dissipation actually produce more fragments than the perfectly elastic baseline, with the total fragment count steadily increasing as the restitution coefficient decreases. This indicates that contact dissipation makes the fragmentation process significantly more efficient at localizing damage and driving cracks to full separation. Since the theoretical energy required to form a single new fragment is exactly the fracture energy G_c , we can quantify the overall efficiency of the fragmentation using the ratio $\hat{\mathcal{G}}/N_f$. It normalizes the actual total fracture energy by the theoretical fracture energy required to produce N_f fragments. As illustrated in Figure 15, this ratio decreases drastically—from ~ 4 in the perfectly elastic case down to ~ 1.8 for $e < 0.999$. Contact dissipation therefore promotes a fragmentation regime that is more than twice as efficient by suppressing energy lost to partially damaged cohesive zones ($d < 1$).

To rationalize this contradiction, we hypothesize that contact dissipation modifies damage localization by filtering wave propagation. In the perfectly elastic case ($e = 1$), stress waves reflect off boundaries and crack faces without attenuation, maintaining a highly vibratory stress field along the bar. This environment promotes diffuse damage growth in many cohesive elements and favors the formation of extended damaged zones rather than clean separations. For $e < 1$, contact dissipation effectively acts as a low-pass filter on the stress field, systematically suppressing high-frequency oscillations and keeping cohesive gaps small. Crucially, this damping mechanism is driven by contact; therefore, its effect scales directly with the number of contact zones. As the material accumulates damage and generates more cohesive interfaces, the increased frequency of contact events accelerates wave attenuation. By filtering out such wave interference, this process allows tensile stresses to localize more stably, promoting clean, localized fractures (see supplemental movies).

However, this phenomenon should not motivate a choice for e without a more detailed understanding of the underlying physics of such a coefficient. In real materials, the restitution coefficient is not constant but a complex function of local dissipation, dependent on the relative contact velocity, surface roughness, and material properties. Future work should aim to characterize this relationship to inform more physically accurate choices for e in fragmentation simulations.

5 Conclusion

In this work, we adapted and validated a novel nonsmooth explicit-implicit time-integration scheme, the nonsmooth Newmark (NSN) method ($\beta = 0, \gamma = \frac{1}{2}$), designed specifically for simulating dynamic fragmentation with nonsmooth unilateral contact. Following [43], the proposed scheme combines the computational efficiency of explicit time integration for bulk dynamics and cohesive fracture with the robustness of the NSCD method for resolving complex contact interactions, while maintaining second-order accuracy during free-flight phases. Through a series of benchmark problems, the NSN scheme demonstrated excellent performance compared to reference solutions and existing nonsmooth methods. For constant acceleration scenarios, such as the bouncing ball test, the method exhibited accuracy comparable to both the implicit Moreau-Jean (MJ) scheme ($\theta = \frac{1}{2}$) and the semi-explicit CD-Lagrange (CDL) scheme. For more complex

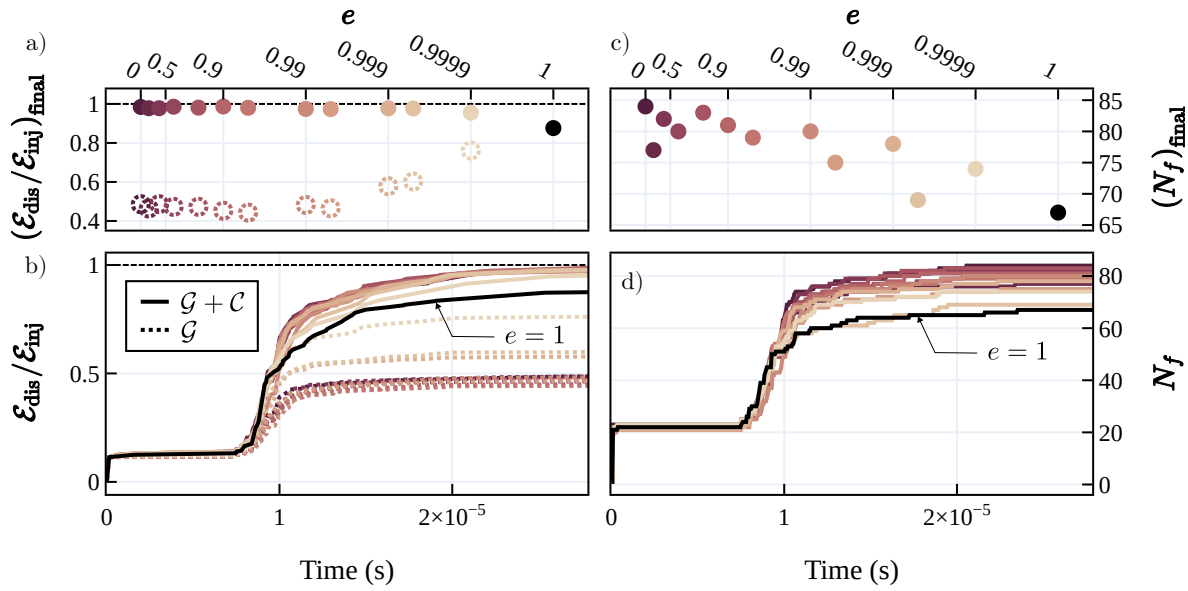


Figure 14: On all subfigures, the color scale shows different values of $e \in [0, 0.9999]$ while black shows the case with $e = 1$. **a)** Final values of the normalized fracture energy $\mathcal{G}/\mathcal{E}_{\text{inj}}$ (dashed circles) and total dissipated energy summing fracture and contact, $(\mathcal{G} + \mathcal{C})/\mathcal{E}_{\text{inj}}$ (solid circles) as a function of e . **b)** Evolution in time of these energies for different restitution coefficients e . Dashed and solid lines follow the same logic as **a)**. **c)** Final number of fragments N_f as a function of the restitution coefficient e . **d)** Evolution in time of the number of fragments for different restitution coefficients e . The results show that while the total dissipated energy $\mathcal{G} + \mathcal{C}$ is essentially independent of e for any inelastic contact ($e < 1$), the number of fragments increases as e decreases, suggesting that contact dissipation promotes damage localization and the formation of fully separated fragments.

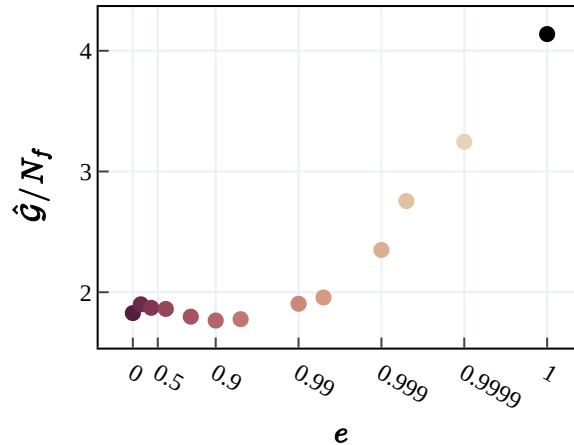


Figure 15: Actual total fracture energy \mathcal{G} normalized by the theoretical fracture energy required to create N_f fragments, $N_f \times G_c$, as a function of the restitution coefficient e . The efficiency of the fragmentation process increases as e decreases, as less energy is required to create more fragments.

impact dynamics, such as a bar striking a rigid wall, the NSN scheme maintained its accuracy (second-order on smooth terms, first order on nonsmooth terms)—matching the CDL scheme and outperforming the degrading MJ scheme—while demonstrating superior robustness to variations in the coefficient of restitution.

To bridge our numerical framework with previous studies detailing the instabilities of penalty-based contact formulations with an explicit approach [30], we analyzed a variant of the impacting bar featuring internal cohesive damage ($d < 1$). Our results confirm that the NSN approach effectively represents the converged solution of the penalty method. Compared with the highest penalty stiffnesses tested, the NSN scheme achieved similar displacement accuracy, improved velocity accuracy, and machine-precision energy conservation. Crucially, the nonsmooth approach eliminated the numerical instabilities inherent to penalty-based methods and exhibited exceptional robustness to time-step variations. While the NSN scheme incurs a per-step computational cost roughly five times that of a purely explicit scheme with penalty-based contact, its

improved stability permits the use of significantly larger time steps, ultimately resulting in a substantial reduction in the overall computational cost for a given accuracy threshold.

Finally, we applied the proposed method to a highly dynamic benchmark: the one-dimensional fragmentation of a bar under a constant strain rate. For free expansion, the method accurately reproduced the expected ZMR predictions for fragment size [24], confirming that the new contact treatment does not artificially influence the results. When the bar's expansion is confined to rigid boundaries, the numerical model successfully captures a fundamental shift in fragmentation physics. Confinement shifts the energy budget available for fracture from the local kinetic energy of individual fragments to the global kinetic energy of the entire system, leading to a drastic increase in fracture energy dissipation and a corresponding reduction in the mean fragment size. Furthermore, the robust enforcement of nonsmooth contact allowed us to uncover counterintuitive dynamics regarding the role of contact dissipation during this confined cascade of spalling events. We demonstrated that decreasing the restitution coefficient e reduces the energy dissipated for fracture but increases the final number of fragments. Introducing contact dissipation helps localize damage and drives cracks to full separation, thereby preventing the system from dissipating energy in distributed, partial damage zones ($d < 1$).

The NSN scheme is also valid for two- and three-dimensional problems. Future work will implement this method in the fully parallelized, high-performance environment of the open-source code `Akantu` [26].

Acknowledgements

This research was funded by the Swiss National Science Foundation (SNSF) [Grant N° 212935].

A Symmetry and positive semidefiniteness of the modified Delassus operator.

To solve the LCP (45) as a constrained quadratic program (49), the modified Delassus operator must be symmetric positive semidefinite (SPSD). We show here that this is indeed the case under the usual explicit dynamics time-step condition. Recall that

$$\mathbf{W}' = \mathbf{H}^A \mathbf{M}^{-1} (\mathbf{H}^A)^\top - \frac{\Delta t^2}{4} \mathbf{H}^A \mathbf{M}^{-1} \mathbf{K} \mathbf{M}^{-1} (\mathbf{H}^A)^\top.$$

We assume throughout that the mass matrix \mathbf{M} is symmetric positive definite (SPD) and the stiffness matrix \mathbf{K} is SPSD.

Symmetry. Since \mathbf{M}^{-1} is symmetric and \mathbf{K} is symmetric,

$$\left(\mathbf{H}^A \mathbf{M}^{-1} (\mathbf{H}^A)^\top \right)^\top = \mathbf{H}^A \mathbf{M}^{-1} (\mathbf{H}^A)^\top,$$

and, by the same argument,

$$\left(\mathbf{H}^A \mathbf{M}^{-1} \mathbf{K} \mathbf{M}^{-1} (\mathbf{H}^A)^\top \right)^\top = \mathbf{H}^A \mathbf{M}^{-1} \mathbf{K} \mathbf{M}^{-1} (\mathbf{H}^A)^\top.$$

Hence \mathbf{W}' is symmetric.

Positive semidefiniteness under the standard time-step condition. For any \mathbf{x} , set $\mathbf{y} := \mathbf{M}^{-1/2} (\mathbf{H}^A)^\top \mathbf{x}$. Then

$$\mathbf{x}^\top \mathbf{W}' \mathbf{x} = \|\mathbf{y}\|^2 - \frac{\Delta t^2}{4} \mathbf{y}^\top (\mathbf{M}^{-1/2} \mathbf{K} \mathbf{M}^{-1/2}) \mathbf{y}.$$

Let λ_{\max} be the largest eigenvalue of the SPSD matrix $\mathbf{M}^{-1/2} \mathbf{K} \mathbf{M}^{-1/2}$ and define $\omega_{\max} := \sqrt{\lambda_{\max}}$. Then

$$\mathbf{x}^\top \mathbf{W}' \mathbf{x} \geq \left(1 - \frac{\Delta t^2}{4} \lambda_{\max} \right) \|\mathbf{y}\|^2 = \left(1 - \frac{\Delta t^2}{4} \omega_{\max}^2 \right) \|\mathbf{y}\|^2.$$

Therefore,

$$\mathbf{W}' \succeq 0 \quad \text{whenever} \quad \Delta t \leq \frac{2}{\omega_{\max}}.$$

This is a *sufficient (not necessary)* time-step condition that ensures the convexity of the QP; it coincides with the standard central-difference bound. In particular, \mathbf{W}' may remain SPSD for larger Δt if the contact subspace does not excite the stiffest mode (the estimate uses the global spectral radius).

B Equivalence of implicit Moreau-Jean and semi-explicit nonsmooth Newmark under constant acceleration

In this section, we demonstrate how the implicit Moreau-Jean (MJ) and the explicit nonsmooth Newmark (NSN) ($\beta = 0$, $\gamma = \frac{1}{2}$) schemes produce identical trajectories for the bouncing ball problem when the gravitational acceleration g is constant and the time step Δt is chosen such that impact detection is synchronized. We assume a constant acceleration $a(t) = -g$, a time step Δt , and a restitution coefficient e . The state at time step n is given by position u_n and velocity v_n .

B.1 Smooth phase (free flight)

Between impacts, the motion is governed purely by gravity.

Moreau-Jean Scheme: The velocity update is explicit Euler:

$$v_{n+1} = v_n - g\Delta t \tag{68}$$

The position update uses the trapezoidal rule:

$$u_{n+1} = u_n + \frac{\Delta t}{2} (v_n + v_{n+1}) \tag{69}$$

Substituting (68) into (69) gives:

$$u_{n+1}^{\text{MJ}} = u_n + \frac{\Delta t}{2} (v_n + v_n - g\Delta t) = u_n + v_n \Delta t - \frac{1}{2} g \Delta t^2 \tag{70}$$

Nonsmooth Newmark scheme: The standard explicit Newmark predictor for displacement with $\beta = 0$ and $\gamma = \frac{1}{2}$ (constant acceleration) is:

$$u_{n+1}^{\text{NSN}} = u_n + v_n \Delta t + \frac{1}{2} a_n \Delta t^2 = u_n + v_n \Delta t - \frac{1}{2} g \Delta t^2 \quad (71)$$

Comparing (70) and (71), the kinematic updates for the smooth phase are identical.

B.2 Impact Phase

By using the respective gap prediction of MJ and nonsmooth Newmark (NSN) schemes, we assume both predictions detect a contact at step $n + 1$. The post-impact velocity is defined by the restitution law $v_{n+1} = -ev_n$.

Moreau-Jean scheme: The position update remains a trapezoidal average of velocities:

$$u_{n+1}^{\text{MJ}} = u_n + \frac{\Delta t}{2} (v_n + v_{n+1}) = u_n + \frac{\Delta t}{2} v_n (1 - e) \quad (72)$$

Nonsmooth Newmark scheme: The NSN scheme first computes the “smooth” predictor values, denoted by ($\tilde{\cdot}$):

$$\tilde{u}_{n+1} = u_n + v_n \Delta t - \frac{1}{2} g \Delta t^2 \quad (73)$$

$$\tilde{v}_{n+1} = v_n - g \Delta t \quad (74)$$

The velocity jump \hat{v}_{n+1} required to satisfy the restitution law is the difference between the target velocity and the predictor velocity:

$$\hat{v}_{n+1} = v_{n+1} - \tilde{v}_{n+1} = (-ev_n) - (v_n - g \Delta t) \quad (75)$$

The final position is updated using the Newmark correction term $\frac{\Delta t}{2} \hat{v}_{n+1}$:

$$u_{n+1}^{\text{NSN}} = \tilde{u}_{n+1} + \frac{\Delta t}{2} \hat{v}_{n+1} \quad (76)$$

Substituting the expressions for \tilde{u}_{n+1} and \hat{v}_{n+1} :

$$u_{n+1}^{\text{NSN}} = \left(u_n + v_n \Delta t - \frac{1}{2} g \Delta t^2 \right) + \frac{\Delta t}{2} (-ev_n - v_n + g \Delta t) \quad (77)$$

With the acceleration terms $\frac{1}{2} g \Delta t^2$ canceling out exactly, expanding the correction term simplifies to:

$$u_{n+1}^{\text{NSN}} = u_n + \frac{\Delta t}{2} v_n (1 - e) \quad (78)$$

Comparing this result with Eq. (72), we see that $u_{n+1}^{\text{MJ}} = u_{n+1}^{\text{NSN}}$. Thus, provided that the contact-detection logic is triggered at the same step, both schemes yield algebraically identical updates.

C Expanding ring simulation parameters

The bar is discretized into N_e linear (P1) bar elements. To improve numerical convergence, the length of each element $h_e = L/N_e$ is randomized uniformly between $\pm 0.4 \times h_e$ as recommended by [57]. To introduce strength variation in the bar, we randomly assign N_{def} defect locations along the bar. At these sites, the cohesive strength is drawn from a uniform distribution $\sigma_{c,\text{def}} \in [0.98, 1] \sigma_c$. The choice of N_{def} is guided by two main criteria:

- **Mesh independence:** By using a fixed number of defect sites rather than varying the strength of every potential interface along the mesh, we prevent the fragment size distribution from becoming mesh-dependent. Without this constraint, refining the mesh would artificially increase the probability of encountering a “weak link” per unit length, potentially shifting the failure mode from localized cracking to non-physical distributed damage [24, 58].
- **Defect spacing:** The number of defects, N_{def} , is selected so that the average spacing between defects is significantly smaller than the expected fragment size at a given strain rate. It ensures that the available defect sites are sufficient to capture the fragmentation process without limiting the number of fragments formed. Consequently, the choice of N_{def} is also dependent on the imposed strain rate.

The domain length L , the mesh density $\rho_e = N_e/L$ and defect density $\rho_{\text{def}} = N_{\text{def}}/L$ are termed converged at a given ($\hat{\epsilon}$) when further refinement of ρ_e (and, respectively, of ρ_{def} at fixed ρ_e/ρ_{def}) produces negligible changes in the number of fragments and in the energy dissipation. To maintain a statistical significance of the results and numerical convergence across the range of strain rates, they are adjusted as follows:

- **Quasi-static regime** ($\hat{\epsilon} \leq 1$): The domain length is set to $L = 10^{-1}\text{m}$, which serves as a representative volume element (RVE) for the lowest strain rate ($\hat{\epsilon} = 10^{-3}$) where fragments are the largest. Specifically, it allows us to capture ~ 100 fragments at this strain rate. The mesh density is converged at $\hat{\epsilon} = 1$, where fragment sizes are the smallest in that regime, resulting in $\rho_e = 5 \times 10^5 \text{m}^{-1}$. Similarly, the defect density is converged at that same strain rate to a value of $\rho_{\text{def}} = 10^5 \text{m}^{-1}$. These values ($L, \rho_e, \rho_{\text{def}}$) are held constant for all $\hat{\epsilon} \leq 1$.
- **Dynamic regime** ($\hat{\epsilon} > 1$): In the dynamic regime, Grady-type scaling and numerical studies indicate that the characteristic fragment size decreases as $\hat{\epsilon}^{-2/3}$. To retain a comparable number of fragments for each strain rate while controlling computational cost, we scale the domain length as $L \propto \hat{\epsilon}^{-2/3}$. At the same time, we increase the mesh density as $\rho_e \propto \hat{\epsilon}^{2/3}$ so that the number of elements per fragment remains approximately constant. Finally, we keep the element-to-defect ratio constant at $\rho_e/\rho_{\text{def}} = 5$. This strategy preserves accuracy and statistical representativity across strain rates while limiting the total number of degrees of freedom.

These simulation parameters are summarized in Table 2.

	Imposed strain rate $\hat{\epsilon}$						
	10^{-3}	10^{-2}	10^{-1}	1	10	10^2	10^3
Bar length, L [m]	10^{-1}	10^{-1}	10^{-1}	10^{-1}	2.15×10^{-2}	4.64×10^{-3}	10^{-3}
Mesh density, ρ_e [m^{-1}]	5.0×10^5	5.0×10^5	5.0×10^5	5.0×10^5	2.32×10^6	1.08×10^7	5.0×10^7
Defect density, ρ_{def} [m^{-1}]	1.0×10^5	1.0×10^5	1.0×10^5	1.0×10^5	4.64×10^5	2.16×10^6	1.0×10^7

Table 2: Simulation parameters for each imposed strain rate.

References

- [1] D. Grady and M. Kipp, “Mechanisms of dynamic fragmentation: factors governing fragment size,” *Mechanics of Materials*, vol. 4, no. 3-4, pp. 311–320, 1985.
- [2] D. Grady, *Fragmentation of rings and shells: the legacy of NF Mott*. Springer Science & Business Media, 2007.
- [3] K. Ramesh, J. D. Hogan, J. Kimberley, and A. Stickle, “A review of mechanisms and models for dynamic failure, strength, and fragmentation,” *Planetary and Space Science*, vol. 107, pp. 10–23, 2015.
- [4] F. Hild, “On characteristic parameters involved in dynamic fragmentation processes,” *Mechanics of Materials*, vol. 80, pp. 340–350, 2015.
- [5] S. I. Abarzhi, A. K. Bhowmick, A. Naveh, A. Pandian, N. C. Swisher, R. F. Stellingwerf, and W. D. Arnett, “Supernova, nuclear synthesis, fluid instabilities, and interfacial mixing,” *Proceedings of the National Academy of Sciences*, vol. 116, no. 37, pp. 18184–18192, 2019.
- [6] J.-C. Liou, S. Clark, N. Fitz-Coy, T. Huynh, J. Opiela, M. Polk, B. Roebuck, R. Rushing, M. Sorge, and M. Werremeyer, “Debrisat-a planned laboratory-based satellite impact experiment for breakup fragment characterizations,” in *6th European Conference on Space Debris*, no. JSC-CN-28456, 2013.
- [7] H. Cowardin, C. Cruz, J. Murray, J. Seago, A. Manis, D. Gates, J. Reyes, and J. Opiela, “Updates on the debrisat hypervelocity experiment and characterization of fragments in support of environmental models,” *International Journal of Impact Engineering*, vol. 180, p. 104669, 2023.
- [8] J. Murray, H. Cowardin, J.-C. Liou, M. Sorge, N. Fitz-Coy, and T. Huynh, “Analysis of the debrisat fragments and comparison to the nasa standard satellite breakup model,” in *International Orbital Debris Conference (IOC)*, no. JSC-E-DAA-TN73918, 2019.
- [9] L. Olivieri, C. Giacomuzzo, and A. Francesconi, “Analysis of fragments larger than 2 mm generated by a picosatellite fragmentation experiment,” *Acta Astronautica*, vol. 204, pp. 418–424, 2023.
- [10] E. Gudowska-Nowak, K. Psonka-Antończyk, K. Weron, T. Elsässer, and G. Taucher-Scholz, “Distribution of dna fragment sizes after irradiation with ions,” *The European Physical Journal E*, vol. 30, no. 3, p. 317, 2009.
- [11] C. Miehe, M. Hofacker, and F. Welschinger, “A phase field model for rate-independent crack propagation: Robust algorithmic implementation based on operator splits,” *Computer Methods in Applied Mechanics and Engineering*, vol. 199, no. 45-48, pp. 2765–2778, 2010.
- [12] G. A. Francfort and J.-J. Marigo, “Revisiting brittle fracture as an energy minimization problem,” *Journal of the Mechanics and Physics of Solids*, vol. 46, no. 8, pp. 1319–1342, 1998.
- [13] N. Chevaugeon and N. Moës, “Lipschitz regularization for fracture: the lip-field approach,” *Computer methods in applied mechanics and engineering*, vol. 402, p. 115644, 2022.
- [14] N. Moës, J. Dolbow, and T. Belytschko, “A finite element method for crack growth without remeshing,” *International journal for numerical methods in engineering*, vol. 46, no. 1, pp. 131–150, 1999.
- [15] D. S. Dugdale, “Yielding of steel sheets containing slits,” *Journal of the Mechanics and Physics of Solids*, vol. 8, no. 2, pp. 100–104, 1960.
- [16] G. I. Barenblatt, “The mathematical theory of equilibrium cracks in brittle fracture,” *Advances in Applied Mechanics*, vol. 7, pp. 55–129, 1962.
- [17] X.-P. Xu and A. Needleman, “Numerical simulations of fast crack growth in brittle solids,” *Journal of the Mechanics and Physics of Solids*, vol. 42, no. 9, pp. 1397–1434, 1994.
- [18] R. Radovitzky, A. Seagraves, M. Tupek, and L. Noels, “A scalable 3d fracture and fragmentation algorithm based on a hybrid, discontinuous galerkin, cohesive element method,” *Computer Methods in Applied Mechanics and Engineering*, vol. 200, no. 1-4, pp. 326–344, 2011.
- [19] V. P. Nguyen, “Discontinuous galerkin/extrinsic cohesive zone modeling: Implementation caveats and applications in computational fracture mechanics,” *Engineering fracture mechanics*, vol. 128, pp. 37–68, 2014.
- [20] G. T. Camacho and M. Ortiz, “Computational modelling of impact damage in brittle materials,” *International Journal of Solids and Structures*, vol. 33, no. 20-22, pp. 2899–2938, 1996.
- [21] M. G. Tijssens, B. L. Sluys, and E. van der Giessen, “Numerical simulation of quasi-brittle fracture using damaging cohesive surfaces,” *European Journal of Mechanics-A/Solids*, vol. 19, no. 5, pp. 761–779, 2000.
- [22] M. Ortiz and A. Pandolfi, “Finite-deformation irreversible cohesive elements for three-dimensional crack-propagation analysis,” *International Journal for Numerical Methods in Engineering*, vol. 44, no. 9, pp. 1267–1282, 1999.
- [23] E. Repetto, R. Radovitzky, and M. Ortiz, “Finite element simulation of dynamic fracture and fragmentation of glass rods,” *Computer Methods in Applied Mechanics and Engineering*, vol. 183, no. 1-2, pp. 3–14, 2000.
- [24] F. Zhou, J.-F. Molinari, and K. Ramesh, “A cohesive model based fragmentation analysis: effects of strain rate and initial defects distribution,” *International Journal of Solids and Structures*, vol. 42, no. 18-19, pp. 5181–5207, 2005.

- [25] A. Pandolfi, P. Krysl, and M. Ortiz, “Finite element simulation of ring expansion and fragmentation: the capturing of length and time scales through cohesive models of fracture,” *International Journal of Fracture*, vol. 95, no. 1, pp. 279–297, 1999.
- [26] N. Richart, G. Anciaux, E. Gallyamov, L. Frérot, D. S. Kammer, M. Pundir, M. Vocialta, A. Cuba Ramos, M. Corrado, P. Müller, *et al.*, “Akantu: an hpc finite-element library for contact and dynamic fracture simulations,” *Journal of Open Source Software*, vol. 9, no. 94, p. 5253, 2024.
- [27] P. Wriggers and T. A. Laursen, *Computational contact mechanics*, vol. 2. Springer, 2006.
- [28] T. A. Laursen, *Computational contact and impact mechanics: fundamentals of modeling interfacial phenomena in nonlinear finite element analysis*. Springer Science & Business Media, 2003.
- [29] C. Kane, J. E. Marsden, M. Ortiz, and M. West, “Variational integrators and the newmark algorithm for conservative and dissipative mechanical systems,” *International Journal for numerical methods in engineering*, vol. 49, no. 10, pp. 1295–1325, 2000.
- [30] T. Ghesquière-Diérckx, J.-F. Molinari, and G. Anciaux, “Stability of extrinsic cohesive-zone model with penalty-based contact in explicit dynamic fragmentation simulations,” *Mechanics of Materials*, p. 105581, 2025.
- [31] J. Hetherington, A. Rodríguez-Ferran, and H. Askes, “A new bipenalty formulation for ensuring time step stability in time domain computational dynamics,” *International Journal for Numerical Methods in Engineering*, vol. 90, no. 3, pp. 269–286, 2012.
- [32] J. Hetherington, A. Rodríguez-Ferran, and H. Askes, “The bipenalty method for arbitrary multipoint constraints,” *International Journal for Numerical Methods in Engineering*, vol. 93, no. 5, pp. 465–482, 2013.
- [33] R. Kolman, J. Kopačka, J. A. González, S. S. Cho, and K. Park, “Bi-penalty stabilized technique with predictor–corrector time scheme for contact-impact problems of elastic bars,” *Mathematics and Computers in Simulation*, vol. 189, pp. 305–324, 2021.
- [34] H. B. Khenous, P. Laborde, and Y. Renard, “Mass redistribution method for finite element contact problems in elastodynamics,” *European Journal of Mechanics-A/Solids*, vol. 27, no. 5, pp. 918–932, 2008.
- [35] Y. Renard, “The singular dynamic method for constrained second order hyperbolic equations: application to dynamic contact problems,” *Journal of Computational and Applied Mathematics*, vol. 234, no. 3, pp. 906–923, 2010.
- [36] J. J. Moreau, “Unilateral contact and dry friction in finite freedom dynamics,” in *Nonsmooth mechanics and Applications*, pp. 1–82, Springer, 1988.
- [37] M. Jean and J. J. Moreau, “Unilaterality and dry friction in the dynamics of rigid body collections,” in *1st Contact Mechanics International Symposium*, pp. 31–48, 1992.
- [38] M. Jean, “The non-smooth contact dynamics method,” *Computer methods in applied mechanics and engineering*, vol. 177, no. 3-4, pp. 235–257, 1999.
- [39] J. J. Moreau, “Numerical aspects of the sweeping process,” *Computer methods in applied mechanics and engineering*, vol. 177, no. 3-4, pp. 329–349, 1999.
- [40] V. Acary and B. Brogliato, *Numerical methods for non-smooth dynamical systems: applications in mechanics and electronics*. Springer Science & Business Media, 2008.
- [41] N. A. Collins-Craft, F. Bourrier, and V. Acary, “On the formulation and implementation of extrinsic cohesive zone models with contact,” *Computer Methods in Applied Mechanics and Engineering*, vol. 400, p. 115545, 2022.
- [42] N. A. Collins-Craft and V. Acary, “On the formulation and implementation of mixed mode i and mode ii extrinsic cohesive zone models with contact and friction.” Preprint, 2025.
- [43] Q.-z. Chen, V. Acary, G. Virlez, and O. Brüls, “A nonsmooth generalized- α scheme for flexible multibody systems with unilateral constraints,” *International Journal for Numerical Methods in Engineering*, vol. 96, no. 8, pp. 487–511, 2013.
- [44] D. Grady, “Local inertial effects in dynamic fragmentation,” *Journal of Applied Physics*, vol. 53, no. 1, pp. 322–325, 1982.
- [45] F.-E. Fekak, M. Brun, A. Gravouil, and B. Depale, “A new heterogeneous asynchronous explicit–implicit time integrator for nonsmooth dynamics,” *Computational mechanics*, vol. 60, no. 1, pp. 1–21, 2017.
- [46] N. J. Carpenter, R. L. Taylor, and M. G. Katona, “Lagrange constraints for transient finite element surface contact,” *International journal for numerical methods in engineering*, vol. 32, no. 1, pp. 103–128, 1991.
- [47] L. Paoli and M. Schatzman, “A numerical scheme for impact problems i: The one-dimensional case,” *SIAM Journal on Numerical Analysis*, vol. 40, no. 2, pp. 702–733, 2002.
- [48] L. Paoli and M. Schatzman, “A numerical scheme for impact problems ii: The multidimensional case,” *SIAM journal on numerical analysis*, vol. 40, no. 2, pp. 734–768, 2002.
- [49] J. Di Stasio, D. Dureisseix, A. Gravouil, G. Georges, and T. Homolle, “Benchmark cases for robust explicit time integrators in non-smooth transient dynamics,” *Advanced Modeling and Simulation in Engineering Sciences*, vol. 6, no. 1, p. 2, 2019.

- [50] V. Acary, “Higher order event capturing time-stepping schemes for nonsmooth multibody systems with unilateral constraints and impacts,” *Applied Numerical Mathematics*, vol. 62, no. 10, pp. 1259–1275, 2012.
- [51] R. F. Kulak, “Critical time step estimation for three-dimensional explicit impact analysis,” Argonne National Lab., IL (USA), 01 1989.
- [52] T. J. Hughes, “A note on the stability of newmark’s algorithm in nonlinear structural dynamics,” *International Journal for Numerical Methods in Engineering*, vol. 11, no. 2, pp. 383–386, 1977.
- [53] V. Acary, “Energy conservation and dissipation properties of time-integration methods for nonsmooth elastodynamics with contact,” *ZAMM-Journal of Applied Mathematics and Mechanics/Zeitschrift für Angewandte Mathematik und Mechanik*, vol. 96, no. 5, pp. 585–603, 2016.
- [54] W. Drugan, “Dynamic fragmentation of brittle materials: analytical mechanics-based models,” *Journal of the Mechanics and Physics of Solids*, vol. 49, no. 6, pp. 1181–1208, 2001.
- [55] F. Zhou, J.-F. Molinari, and K. Ramesh, “Effects of material properties on the fragmentation of brittle materials,” *International journal of fracture*, vol. 139, no. 2, pp. 169–196, 2006.
- [56] L. Glenn and A. Chudnovsky, “Strain-energy effects on dynamic fragmentation,” *Journal of applied physics*, vol. 59, no. 4, pp. 1379–1380, 1986.
- [57] J.-F. Molinari, G. Gazonas, R. Raghupathy, A. Rusinek, and F. Zhou, “The cohesive element approach to dynamic fragmentation: the question of energy convergence,” *International Journal for Numerical Methods in Engineering*, vol. 69, no. 3, pp. 484–503, 2007.
- [58] S. Levy and J.-F. Molinari, “Dynamic fragmentation of ceramics, signature of defects and scaling of fragment sizes,” *Journal of the Mechanics and Physics of Solids*, vol. 58, no. 1, pp. 12–26, 2010.